Portland State University

PDXScholar

Dissertations and Theses

Dissertations and Theses

5-20-2021

Photoemission Electron Microscopy for Direct Observation of Photonic and Plasmonic Phenomena

Theodore Stenmark
Portland State University

Follow this and additional works at: https://pdxscholar.library.pdx.edu/open_access_etds

 Part of the Physics Commons

Let us know how access to this document benefits you.

Recommended Citation
Stenmark, Theodore, "Photoemission Electron Microscopy for Direct Observation of Photonic and Plasmonic Phenomena" (2021). *Dissertations and Theses.* Paper 5700.
https://doi.org/10.15760/etd.7572

This Dissertation is brought to you for free and open access. It has been accepted for inclusion in Dissertations and Theses by an authorized administrator of PDXScholar. Please contact us if we can make this document more accessible: pdxscholar@pdx.edu.

Photoemission Electron Microscopy for Direct Observation of Photonic and Plasmonic Phenomena

by

Theodore Stenmark

A dissertation submitted in partial fulfillment of the
requirements for the degree of

Doctor of Philosophy
in
Applied Physics

Dissertation Committee:
Rolf Könenkamp, Chair
Andres LaRosa
Pui-Tak Leung
Shankar Rananavare
Dean Atkinson

Portland State University
2021

© 2021 Theodore Stenmark

Abstract

Photoemission electron microscopy (PEEM) is a high-resolution microscopy technique that collects photoemitted electrons from the sample surface to form an image. PEEM offers a non-scanning imaging method with a spatial resolution in the range of 5-100nm by combining the advantages of light excitation and electron imaging. Our work looks at PEEM as an analysis tool for photonic and plasmonic phenomena. Photonic wave guiding structures exhibiting a strong dispersion relation have attracted considerable attention for applications in integrated optics, communications and sensing devices. Line defects in a photonic crystal (PC) slab offer a highly efficient way to create light with group velocities much smaller than is achievable in uniform materials. Slow light is needed for numerous device applications involving non-linearity in absorption, transmission and reflection, and optical buffers. Propagation velocities in PC waveguide structures are typically measured with interferometric methods involving the outcoupling of the slow light into an optical fiber and comparing its phase delay to a reference light wave. Direct imaging of the modes in the defect, however, is more challenging. Here we present a new approach for direct imaging of defect modes in PEEM.

Metallic nanoparticles are another area of interest due to their plasmonic properties. They exhibit localized surface plasmon resonances (LSP) at particular excitation frequencies depending on their size, shape, and material and are used in a wide variety of applications in medical tagging, sensing, solar cells, and optical coupling. As we move

toward nanoscale devices it becomes critically important to be able to understand and measure not only bulk properties, but also the resonances of individual and small groups of nanoparticles. PEEM is a promising candidate for evaluating such systems due to its noninvasive measuring mechanism and nonlinear response to surface plasmon excitation. Here we report observation of avoided level crossing due the hybridization of the dipolar dimer mode and the single nanoparticle substrate mediated mode in 45nm silver nanoparticle dimers on an indium tin oxide (ITO) substrate with interparticle gaps ranging from 1nm-10nm. By changing the polarization and direction of incidence of the exciting beam the strong coupling can be switched on and off and different resonant modes of the dipole excited. If the substrate is changed to be conductive charge can flow from one particle to the other and an additional charge transfer plasmon (CTP) mode can be excited. These results demonstrate the importance of substrate effects on plasmonic nano-systems and that interparticle coupling can quantitatively be studied on the nanometer scale in PEEM.

Acknowledgments

I would like to thank the many people who helped me on my way throughout graduate school. In particular my advisor, Dr. Könenkamp for his patience and guidance and Dr. Word for his invaluable training and advise.

Table of Contents

List of Tables

List of Figures

Glossary

PEEM: Photoemission Electron Microscopy/Microscope

LEEM: Low Energy Electron Microscopy

SEM: Scanning Electron Microscope

FIB: Focused Ion Beam

ITO: Indium Tin Oxide, a dielectric substrate used in our samples

TE: Transverse Electric

TM: Transverse Magnetic

PC: Photonic crystal

LSP: Localized Surface Plasmon.

NP: Nanoparticle

LDM: Longitudinal Dipolar Mode. The dipolar mode with oscillation of the electron density parallel to the substrate

LSM: Longitudinal Single sphere Mode. The single sphere mode with oscillation of the electron density parallel to the substrate

TSM: Transverse Single sphere Mode. The single sphere mode with oscillation of the electron density perpendicular to the substrate.

1 Introduction

1.1 Motivation and Goals

As development of modern technologies push demand for devices that are ever shrinking in scale, control of photons and electrons and their interactions on the nanoscale is of ever-increasing importance for future innovation. Various interactions between plasmonically excited metals and optically active semiconductors have been identified and are being targeted for chemical and photovoltaic energy conversion, novel lasers [1], [2], and contribute towards the goal of optical control [3], [4]. The effective confinement of electromagnetic fields in plasmonic materials opens the possibility of subwavelength lasers [5] and nano-diodes[6], key components for realizing optical circuits and for quantum computing [7], [8].

Integrated circuits are instrumental in modern computing, the ability to combine billions of electronic components into a single compact package is what allows for the computing power available today. This abundance of processing power is a key driver in science, from computational chemistry to simulation of optical systems, our understanding of the world is increasingly being driven by computer simulations. Computer modeling even promises advances in vaccine development [9], the limits of what is possible expands with computational power. Most computing today is done through manipulation of electrons; an alternate method is photonic computing replacing the electronic signal with photonics. We already transmit information using

photons through fiber optics, which is magnitudes faster than the electronic equivalent, the same would theoretically be true for a photonic computation. The individual components analogues to electronic circuits exist, photonic transistors [10], [11], photonic crystal waveguides which act as wires, etc, but the integration and miniaturization is not yet sufficient to compete with conventional computing.

For photonic computing to become a reality we need the ability to miniaturize photonic components and produce photonic integrated circuits. Plasmonics provide a mechanism to concentrate electromagnetic fields past the optical diffraction limit into volumes with sub wavelength dimensions and offers exciting opportunities for the manipulation and control of light on a nano-meter scale [12], [13]. Photonic crystals allow for control of light propagation. Slow light is needed for numerous optical components requiring non-linearity in absorption, transmission and reflection, and optical buffers which need to delay light pulses and temporarily store optical information for control of dataflow and synchronization. By slowing down the speed of light the time it spends in a location is also lengthened enhancing the light matter interaction. Propagation velocities in photonic crystal waveguide structures can produce these effects and photonic waveguides have become vital components for photonic circuits.

Our work is on the basic sciences side of research where we seek to understand some of the fundamental physics and interactions necessary to achieve these new technologies. Fully understanding plasmonic responses of simple plasmonic resonators and having the

tools to measure plasmonic and photonic responses of real-life physically realizable systems is vital to the success of future applications. In this dissertation we present a direct imaging method for measuring photonic modes of slab waveguides and photonic crystal defect modes as well as substrate dependent measurements of plasmonic modes in nanosphere resonators using photoemission electron microscopy (PEEM).

1.2 Introduction to PEEM

Photoemission Electron Microscopy (PEEM) is a microscopy technique that utilizes the photoelectric effect to probe the surface of a sample. Photoemitted electrons, produced by the interaction of photons from a light source that interact with the sample, are collected to form an image. The idea for imaging with photoelectrons is credited to Brüche who published his initial results using an early design of a magnetic lens in 1933 [14]. It was not until much later when ultra-high vacuum became readily available that PEEM developed into the powerful microscopy technique it is today. Ernst Bauer was an instrumental figure in the field of surface microscopy and is credited with the invention of Low Energy Electron Microscopy (LEEM) [15], [16] which uses low energy electrons to probe sample surfaces. The surge of interest in surface science as well as Bauer's work on electron cathode lenses helped to drive development of PEEM. Early ultra-high vacuum work in PEEM was done at PSU and UO [17] where Griffiths and Rempfer designed and built instruments with spatial resolution down to 10nm, Rempfer being the expert in developing the necessary electron optics. Rempfer at PSU and Rose in Germany also developed concepts for aberration correction in electron optics [18]–[20].

The PEEM used by our laboratory is an aberration corrected microscope based on Rempfer's earlier work. The microscope was designed and constructed in-house [21] in an effort led by Könenkamp, Word and Rempfer, and demonstrated a spatial resolution of 5.4nm in 2010 [22].

The key component to aberration correction in our electron optics is an electron mirror which is designed to counteract some of the optical aberrations in the system. Aberrations occur in electron optical imaging when electrons originating from the same point on the sample end up at different points on the detector despite optimized focusing. Electron lenses produce both spherical and chromatic aberrations. Spherical aberrations are the result of the focal point produced by the peripheral region of the lens field being different from that of the center region. This effect presents itself in light optics in spherical lenses (thus the name) but is also present in electron optical lenses such as those on our microscope. Chromatic aberrations arise in light optics due to the variations of the refractive index of materials with the wavelength of light. The different energy photons then travel through the optical lens on different paths and at varying speeds resulting in different focal lengths for different energy photons. This is analogous to different electron energies traveling through an electron lens being focused at different focal points. The greater the speed of the electron traveling through the electron lens the greater the focal length as in Figure 1.1.

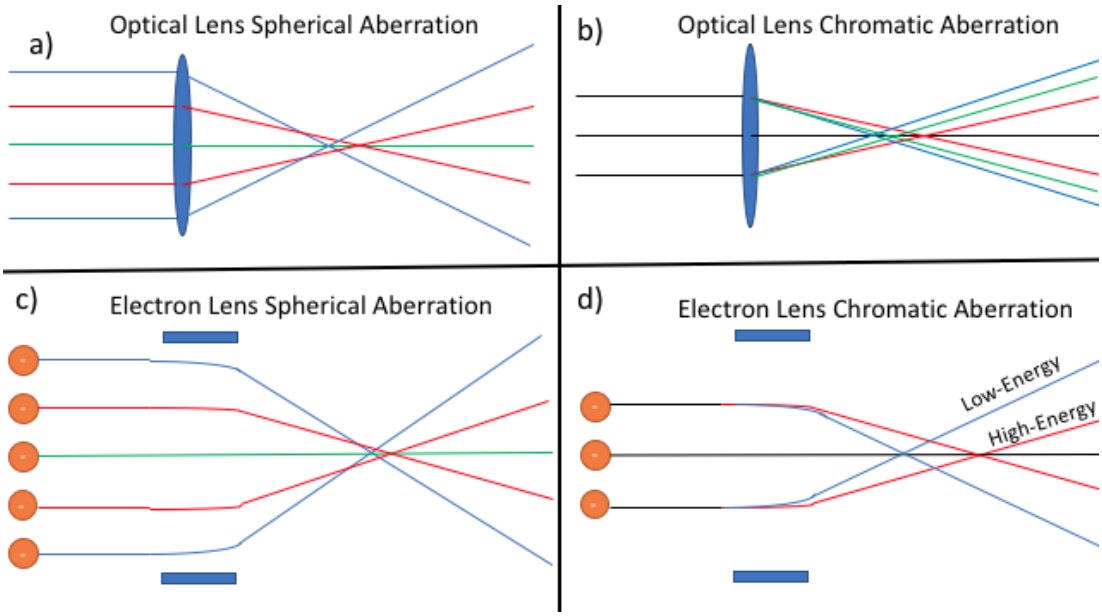

Figure 1.1: a, b) spherical and chromatic aberrations in optical lenses. c, d) Spherical and chromatic aberrations in electron lenses.

Electron optics have an additional source of aberration not present in light optics due to the acceleration field. In our PEEM photoemitted electrons come off the sample surface at low energy ~1eV and are accelerated to 20keV over a distance of a few millimeters. Variations in direction and kinetic energy of the electrons leaving the sample lead to different paths through the acceleration field and additional spherical and chromatic aberration contributions, as shown in Figure 1.2. The electron mirror in our system is a two-electrode mirror which allows for correction of the aberration due to the acceleration field and lenses. In a diode mirror the correction of chromatic and spherical aberrations works best at only one magnification [23].

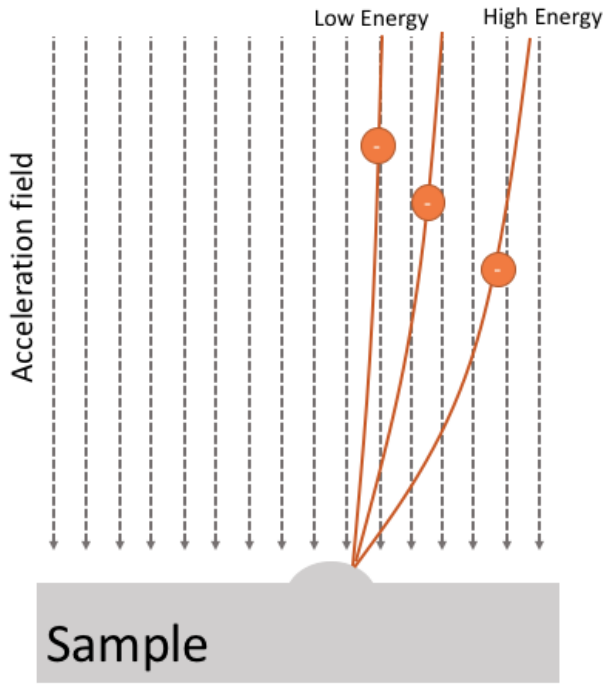

Figure 1.2: The differing angles and energies of the photoemitted electrons leads to differing paths through the acceleration field producing aberrations.

PEEM images can be taken with a mercury lamp as a photon source which provides an incoherent ultraviolet (UV) illumination. The energy of a photon in the UV generally produces single photon emission, that is it only takes the energy of a single photon for the excitation of a photoelectron. In the past decades lasers and synchrotrons have become more powerful photon sources for PEEM and can be advantageous thanks to high power, wavelength tunability, and coherence. In our lab we can illuminate with a mercury lamp, a continuous wave 244nm laser light from a Lexel 95 ion laser, or Spectra-Physics Mai Tai Ti:sapphire pulsed laser illumination at ~800nm or ~400nm , ~266, and ~200nm when sent through frequency multipliers. The photon energies at 400nm and 800nm wavelengths require a multiphoton process for most materials in

order to produce a single photoelectron. The photoemission yield is drastically reduced for these multiphoton processes; however, the high intensity of the laser pulses still produces enough photoemission for imaging with extended exposure times.

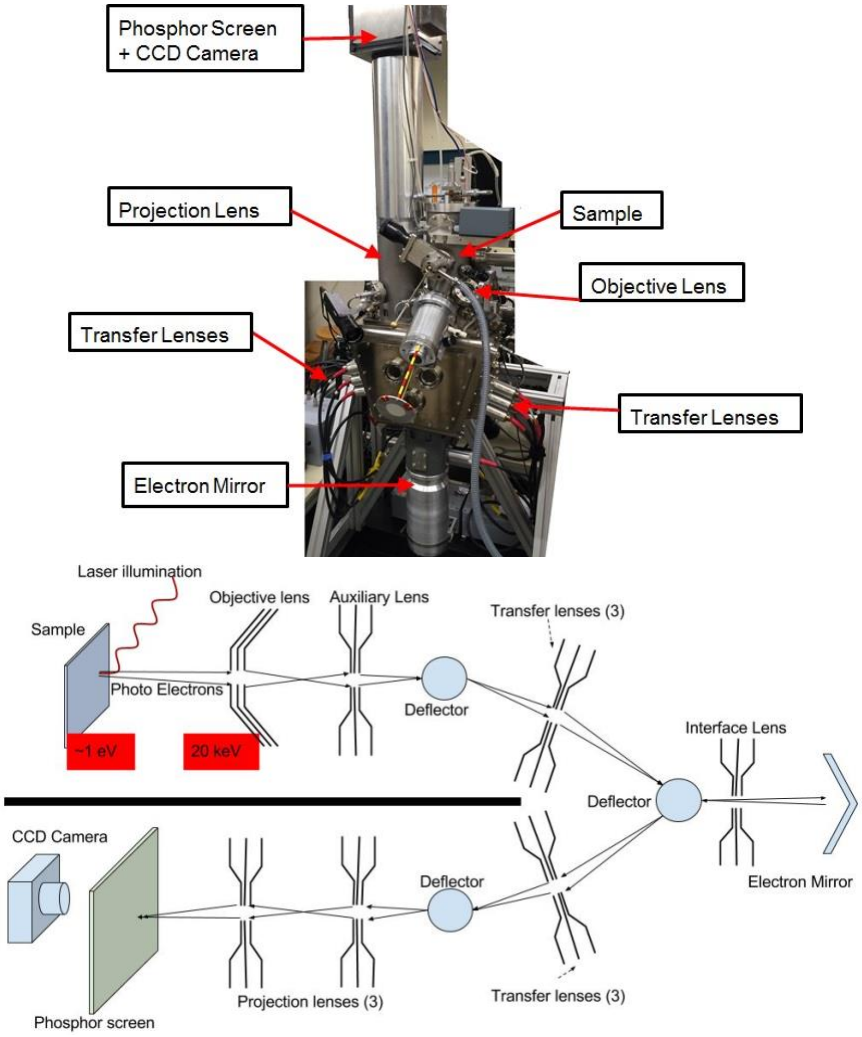

Figure 1.3: a) Image of our photoemission electron microscope and b) a simple diagram of the electron optics. Laser light enters through a port on the back of the microscope and hits the sample exciting photo-emitted electrons. These electrons are accelerated through a potential difference of ~20keV and guided through the electron optics to a phosphor screen where a CCD camera records the image. An electron mirror in the electron optics is used to counteract the aberrations introduced by the electron lenses and the accelerating field.

Contrast in PEEM images comes from the spatial variation of the yield of photoemitted electrons. To produce photoemission an electron must absorb a photon, travel to the surface of the sample, and be ejected into the vacuum. There are several mechanisms that contribute to the probability of photoemission, the work function and electronic structure of the materials in the sample, the topography of the sample, the photon density and absorption depth, the electron density, and the mean free path of the electrons. The fewer number of photons required to overcome the work function of a material, the higher the rate of photoemission from that material [24]. The greater the availability of electrons in a material that can be photoemitted the higher the rate of photoemission. This may vary from material to material depending on the band structure and Fermi level.

A higher photon density, either due to increased illumination intensity or due to photonic resonance modes in the sample, increases the probability that an electron will absorb a photon and thus increases the rate of photoemission. Variations in the electron density, as can be produced from plasmonic responses, produce varying contrast in PEEM. There is some debate over the exact mechanism responsible, i.e. the plasmon density, electron density, and photon density may, in principle, all contribute to the photoemission. No matter the mechanism, photoemission from both photonic and plasmonic responses correlates with the square of the magnitude the electromagnetic field. Since photoemitted electrons originate from the top 5-10nm of the sample surface, in simulations of photonic and plasmonic systems we consider the

photoemission observed in PEEM to be a function of the electric field at the material-vacuum interface of the simulated geometry.

PEEM has been used in a wide array of experiments. Biological applications include the study of cell surfaces and DNA strands [25] as well as potential for characterizing biological samples that have been tagged with highly emitting materials such as Au or Cs [26], [27]. PEEMs equipped with deep UV and x-ray photon sources [28] can probe the magnetic structure of a sample [29], [30] with temporal resolution available using a pump-probe methodology [31]. Angle-resolved photoemission electron spectroscopy (ARPES) can be performed in microscopes equipped with an electron energy analyzer. Another area of interest for PEEM in the last two decades has been the study of plasmonics. PEEM, due to the high sensitivity of photoemission to electromagnetic field intensities, has been demonstrated to be a useful tool for observing a variety of plasmonic responses. Using a pump probe method propagating SPPs have been observed on gold substrates [32]–[36]. PEEM has also been used to characterize a variety of resonant plasmonic structures such as bowtie antennas [37]. Our group previously demonstrated PEEMs ability to image modes of circular patch antennas [38], [39] and to explore and develop device applications [40].

Less explored are the applications of PEEM for analysis of photonic structures. In the past few years our group has demonstrated measurement of optical diffraction [41] and photonic slab waveguide modes [42], [43] as well as the polarization dependence of

coupling between photonic waveguide modes and plasmonic resonances of single nanoparticles [44]. The main focus of my research has been to expand the applications of PEEM in photonics and plasmonic to characterize more complex structures and phenomena [45]–[47]. I have a particular interest in the frequency dependence of photonic modes in photonic crystal waveguides and substrate mediated plasmonic interactions between small groups of nanoparticles. Understanding of these nanoscale plasmonic and photonic systems is essential for development of future technologies and PEEM has as of yet untapped potential to make significant contributions to the field. In this dissertation I present my experimental measurements of plasmonic and photonic phenomena in PEEM.

2 Experiments and Experimental Methods

2.1 Photon Source

The primary photon source used for all experiments consisted of a Spectra-Physics Mai Tai Ti:sapphire laser with 60fs pulse duration at a repetition rate of 100MHz and a Del Mar second harmonic generator to up-convert the fundamental infrared pulses to the near UV range incident on the sample at an angle of 60°. The harmonically doubled pulse has a spectral width of ~4nm at FWHM. The energy of the 400nm wavelength photons requires a 2-photon process to produce photoemission in both silver and ITO, the primary materials in our samples. The laser has an output power of 800mW and a spot area of ~$(40um)^2$ on the sample.

The contrast in a PEEM image comes from differences in material, topography and photon and electron density. When given a relatively flat an uniform material the primary contrast mechanisms comes from variations in photon density and electron density whose contributions to photoemission can both be expressed in terms of the square of the electromagnetic field. The yield of photoelectrons is proportional to the electromagnetic field to the power of $2m$, where m is the number of photons required to produce a single photoelectron,

$$YPE \propto ||E_{tot}||^{2m}. \quad (2.1)$$

The probability of photoemission can be understood as the probability of a photon interacting with an electron which is proportional to the square of the electric field. For

a multiphoton process the electron must interact with two-photons simultaneously, three photons simultaneously for a three-photon process, and so on. This can be described mathematically as the probability of a single photon interacting to the m_{th} power, giving the probability of *m* photons interacting. This non-linearity produces a high contrast between areas of differing photon and electron density. The coefficient of proportionality greatly decreases for higher photon processes requiring longer exposure times to produce an image.

Additional images of samples were taken with a Lexel 95 ion laser which produces CW 244nm illumination with a power output of ~0.1 W. At 244nm the energy of the photons is sufficient for a one photon process. The greater photoemission from a 1-photon process allows for a much lower exposure time and this illumination source is used for focusing the microscope and obtaining higher resolution images of the sample topography.

2.2 Photonic Waveguides

Our photonics work has focused on characterization of photonic waveguide modes based on an interferometric approach [42], [43], [45], [46]. To create the wave-guiding structure we use a sample consisting of a 0.2mm borosilicate glass slide covered with a 280nm ± 20nm thick indium-tin-oxide (ITO) layer. ITO has the advantage of being both transparent in the optical wavelength range, a necessity to create an optical waveguide,

and conductive, a requirement to mitigate charging when imaging in PEEM. ITO has a refractive index of n~2.1 at 400nm. The lower refractive indexes of the glass substrate, n~1.5, and the vacuum superstrate can confine light within the ITO layer through total internal reflections. This forms a slab waveguide that will allow specific modes to propagate through the ITO layer, the exact nature of the mode depends on the refractive indexes of the materials, thickness of the ITO, as well as the frequency of the light, as discussed in ref. [43]. In order to excite the guided modes, we need to couple the light into the ITO layer. We do this with a trench milled into the ITO layer with a FEI Strata 273 focused ion beam (FIB). The incident light is diffracted off the edge of the trench allowing it to couple into the thin film waveguide formed by the ITO layer, the incident light then interferes with the guided mode producing a standing interference pattern as depicted in Figure 2.1.

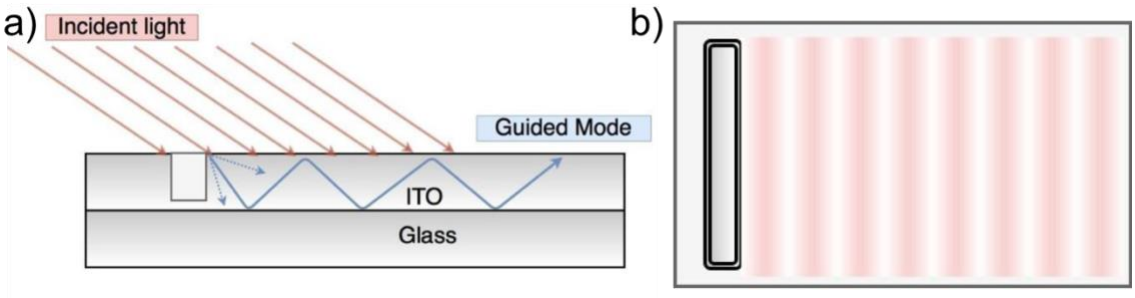

Figure 2.1: a) Basic waveguide experiment: polarized light is directed towards the milled slit at an incident angle of 60°. Interference between the wave-guided light and the non-scattered light produces an interference pattern. b) Schematic of the top down view of the interference pattern produced.

A polarization plate was used to select TE polarization for the incident pulse. A series of images was taken at wavelengths in the range 390nm<λ<410nm with step size between

0.5 and 1nm. For ITO it takes a two-photon process at for light with wavelength of 400nm to produce a photoelectron. The non-linearity of the 2-photon photoemission process gives strong contrast between areas of high and low electromagnetic field intensity.

2.3 Photonic Crystal Waveguide

A more complex waveguiding structure can be created by patterning a slab waveguide with a periodic structure. The periodic changes in refractive index can affect the propagation of photons similar to how electrons interact with ionic lattices in crystalline solids. These photonic structures are known as photonic crystals (PC) and will be discussed in more detail in section 4.2. By leaving a line defect in periodic structure a waveguide can be produced whose guided modes are dependent on the parameters of the photonic crystal lattice.

We created a photonic crystal defect waveguide by milling a triangular lattice of holes into a 280nm ± 20nm thick ITO thin film on glass substrate using FEI strata 273 focused ion beam forming a 2D thin film PC structure. ITO has the advantage of being optically transparent in our available laser excitation range, being conductive which is necessary to mitigate charging, and being readily commercially available. The periodicity of the lattice is 180nm with an approximate hole-diameter of 90nm and extending approximately 90nm into the glass substrate. The photonic crystal structure had a single row of missing holes in the K- Γ direction of the reciprocal lattice forming a linear defect

waveguide as seen in Figure 2.2. A trench was milled perpendicular to the defect to provide a coupling mechanism for the incident light into the defect via diffraction. Due to drift in the FIB processing the coupling trench is ~2 degrees off of perpendicular to the PC defect. We have ITO with refractive index ~2.1 resting on a glass substrate with refractive index ~1.5 and vacuum above to form an asymmetric slab waveguide. A series of images was taken at wavelengths in the range 390nm<λ<410nm with step size between 0.5 and 1nm.

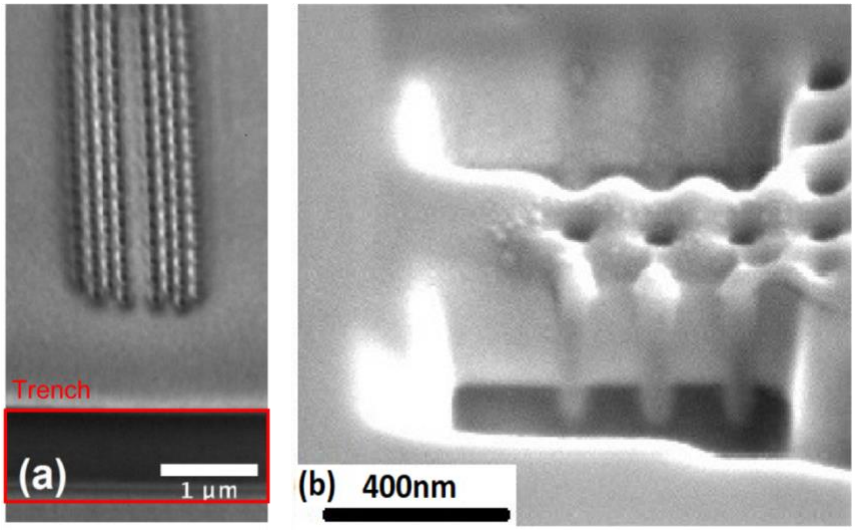

Figure 2.2: (a) PEEM image of periodic structure with CW illumination at 244nm. (b) Cross sectioned example of typical holes milled by the FIB.

2.4 Plasmonic Nanospheres

To construct systems of plasmonic nanoparticles, we purchased citrate capped silver nanoparticles in 2mM aqueous sodium citrate from Sigma Aldrich and deposited them by submerging substrates consisting of ~280nm thick ITO thin film on borosilicate glass purchased from SPI supplies in the nanoparticle solution for periods of 4, 12, 24

and, 48 hours to allow the spheres to adhere to the substrate. Upon removal the substrates were blow-dried with nitrogen. The scanning electron microscope (SEM) in a Helios dual beam FIB was used to identify the deposition time that produced a sample with an appropriate distribution of silver nanoparticles that contained a variety of dimer geometries produced at random by the deposition procedure. The 24-hour submersion produced the most uniform sphere distribution with sufficient density without excessive clumping of the spheres. The sample was then moved to the PEEM for characterization of the spectral and polarization dependent response of the silver nanospheres.

A half-wave polarization plate was used to select the polarization for the incident pulse. Here we define the polarization with respect to the substrate with TE polarization having the electric field of the incident beam parallel to the substrate and TM polarization having the magnetic field parallel to the substrate. Images were obtained with excitation wavelengths from 390nm-445nm at 2.5nm intervals with TM polarization. The average of the brightest 50 pixels of each dipole or individual sphere was taken which correlates directly to the rate of photoemission from that particular sphere geometry.

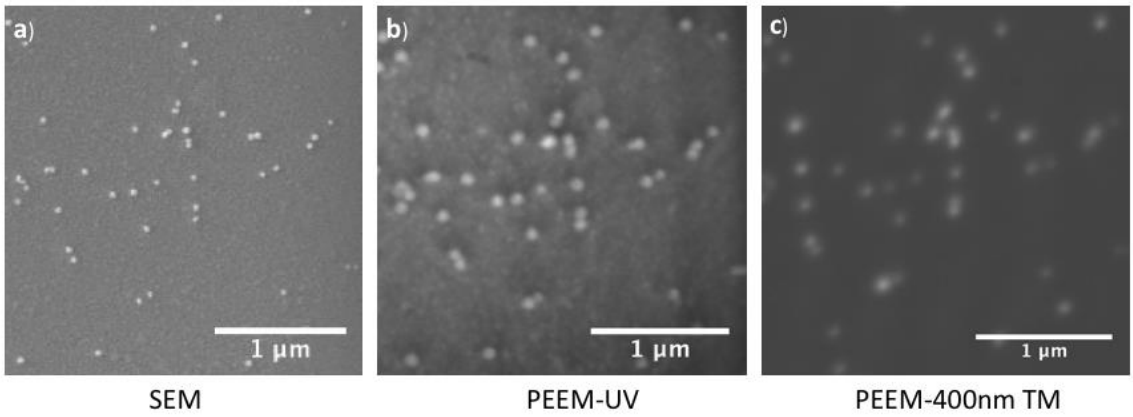

Figure 2.3: Images of a portion of the sample. a) SEM image. b) PEEM image with 244nm CW laser illumination. c) PEEM image with 400nm pulsed laser illumination and TM polarization.

With the pulsed laser at 400nm the resolution in PEEM is insufficient to fully resolve the individual spheres in dipolar pairs. Our typical resolution of an image with photoemission that requires a 2-photon process is on the order of 30-100nm [48], considerably larger than the gap size between the dipoles. The spheres also have a curved topography, the electric field has varying directions at the metal interface of the nanoparticle, tending to give a lateral component to the velocity of the photoemitted electrons making the spheres appear slightly enlarged. Additionally, the greatest electric field is produced in the gap between the spheres producing the greatest photoelectric yield from the edge of the sphere facing the interparticle gap due to the plasmonic field enhancement in the gap region. The greatest photoemission being from the center of the dipole causes a bright region between the spheres which inhibits resolving the individual sphere in a dipole under 400nm illumination as seen in Figure 2.4.

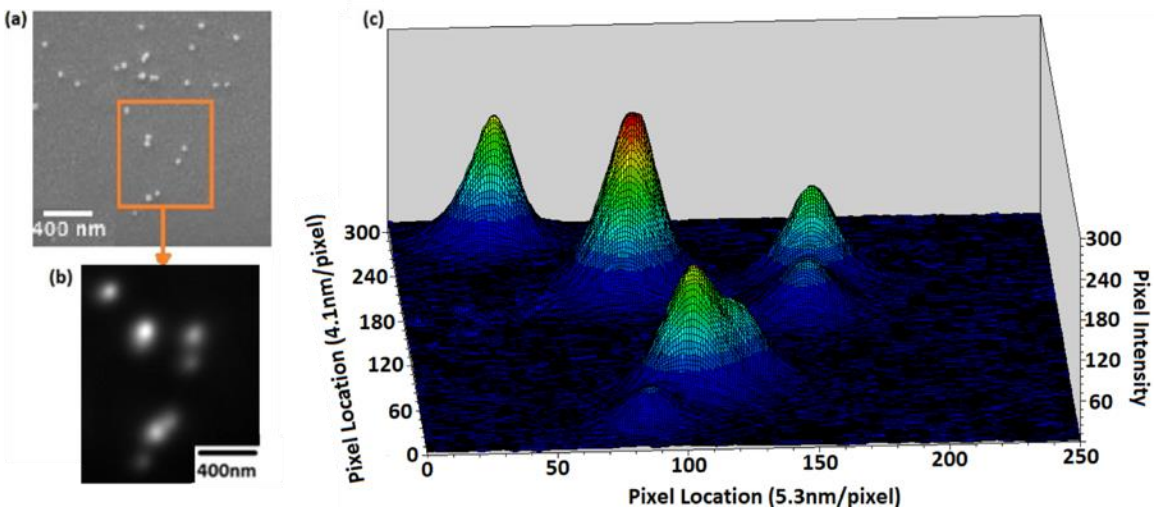

Figure 2.4: (a) SEM image of the silver sphere deposition on ITO. (b) PEEM micrograph taken at 420nm illumination. (c) Plot of pixel intensity vs position for the PEEM image. Greatest brightness occurs at the center of the closely spaced dipole.

There also must be some consideration to the possibility of photons produced via electron field emission. Under sufficiently strong electric fields electron emission can be induced from the sample surface [49]. Areas of high electric field occur in gaps between nanoparticles as well as nanoparticles and the substrate, and previously have been attributed as a source of electron field emission in PEEM in a study of gold spheres on a gold substrate [50]. The field emitted electrons are able to escape the gap between the sphere and the substrate through the pondermotive force which is the force experienced by a charged particle in a nonuniform oscillating electric field which tends to move the particle towards areas of weaker field space. In this case the laser produces the oscillating field moving the field emitted electron out of the gap between the sphere and substrate allowing them to contribute to the PEEM image. The dimensionless

Keldysh parameter [51] is used as an indicator if field emission or photoemission is the dominant process for electron emission given by

$$\gamma = \omega\sqrt{2\mathrm{m}\Phi}/eE, \tag{2.2}$$

where ω is the angular frequency, *E* is the electric field strength, *e* is the charge of an electron and Φ is the work function. When the Keldysh parameter is less than 1, field emission is the dominant mechanism for electron emission and when it is greater than 1 photoemission dominates. Using an estimate of electric field of 60MeV/m for the laser pulse based on the output power, repetition rate, and spot size it would require an enhancement of the electric field of over 400 times in the silver-ITO gap region to produce a keldysh parameter of < 1, a factor 10 higher than the enhancement factor seen in simulation. We estimate the parameter to be between 10-50 indicating that photoemission is strongly favored over field emission in our experiments.

There is some variation in the laser intensity incident on the sample due to tuning of the harmonic doubler, reflectivity of the mirrors in the optical path, centering of the laser spot on the sample, and temporal variations in the laser output power. To account for these variations in laser power between images the rate of photoemission from the spheres is normalized with respect to the photoemission yield from the ITO substrate. ITO and silver both require 2-photon photoemission process in the wavelength range of 390nm-440nm and thus are expected to have a similar response to variation in laser power. The estimated uncertainty of the normalized photoemission is ±4%.

To confirm reproducibility of the spectral response the spectral collection was repeated 3 times as seen in Figure 2.5. The average of the spectra was taken as the final spectral response. The sample was then rotated 90degrees and the process repeated to excite the dipolar plasmonic responses from a different angle. Additionally, images were obtained for different polarizations rotating a quarter wave plate through 90 degrees at 5-degree intervals for an excitation wavelength of 420nm. This goes through a cycle of TM->TE->TM. Similar to the frequency sweep data the polarization dependent response is normalized with respect to the photoemission of the ITO substrate.

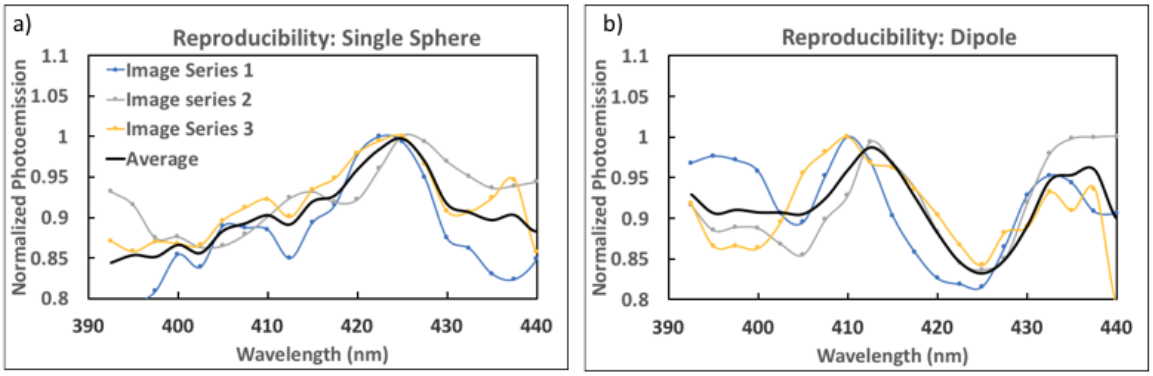

Figure 2.5: a) The photoemission from an individual sphere is extracted from images taken over the available spectral range of the laser. Three series of images are taken and the spectra are averaged. b) The photoemission from a dipole that is excited on axis is extracted from images taken over the available spectral range of the laser. Three series of images are taken and the spectra are averaged.

The peak wavelengths of the experimentally measured plasmonic resonances are determined by fitting the normalized spectral response to a sum of gaussian curves. The peak of the single sphere resonance is expected to correspond to the size of the sphere while the peaks in the dipolar sphere correspond to the dipolar mode and single sphere modes.

3 FEM and FTDT Calculations

3.1 Slab Waveguides

Simulations were conducted in COMSOL Multiphysics, an iterative finite element method (FEM) program, to compare to and verify the experimental results. For the slab waveguide there is symmetry in the y-z plane perpendicular to the ITO layer, which allows for a 2D simulation of the system. An electromagnetic field is defined incident on an ITO layer with a coupling trench. Since the electrons collected in PEEM come from the top 5-10nm of the sample, the time averaged electric field at the surface of the ITO will correlate to the spatial distribution of photoemission in PEEM. A line graph of the square of the normalized electromagnetic field at the ITO surface is used to compare to the experimental results. The normalized electric field is expressed in COMSOL as

$$E_{norm} = \sqrt{E_x^2 + E_y^2 + E_z^2}, \tag{3.1}$$

where *Ex*, *Ey*, and *Ez*, are the real parts of the E-field matrix. The square of normalized electric field is taken to correlate to the photoemission yield in PEEM.

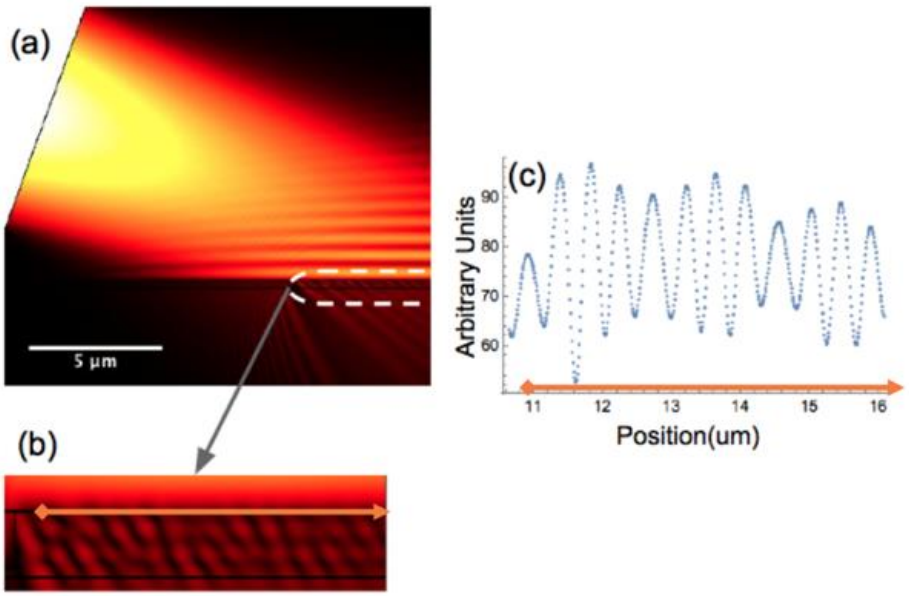

Figure 3.1: (a) Overview for a 2D simulation of the cross-section slab waveguide showing $|E|^2$. (b) Close up of the cross section of the ITO guiding region. (c) Line graph of $|E|^2$ taken at the surface of the ITO thin film waveguide.

3.2 Photonic Crystal Waveguides

Our simulation setup for the photonic crystal waveguide mimics the experimental setup with an electromagnetic wave incident on an ITO layer on glass with a trench to couple into the guided modes in the ITO layer and photonic crystal defect as shown in Figure 3.2. There is no longer the necessary symmetry to reduce the simulation to a 2D problem as in a slab wave guide and a 3D treatment is necessary. A scattering boundary condition is used in the simulation boundaries defined as

$$\boldsymbol{n} \cdot (\nabla E_z) + i\, k_0 E_z = 0, \tag{3.2}$$

where *n* is the normal of the surface and E_z is the electric field. This is an approximation of the Sommerfeld radiation condition. This boundary condition produces a fully nonreflective boundary when a plane wave is incident normal to the boundary. As the

wave approaches a grazing incidence the reflectivity of the boundary increases. The geometry of the simulation boundaries is chosen to minimize these boundary reflections. The minimal reflections that do occur are of little concern as the primary information desired from the simulation is the periodic spacing of the mode seen in the defect channel which is not altered by any back reflections.

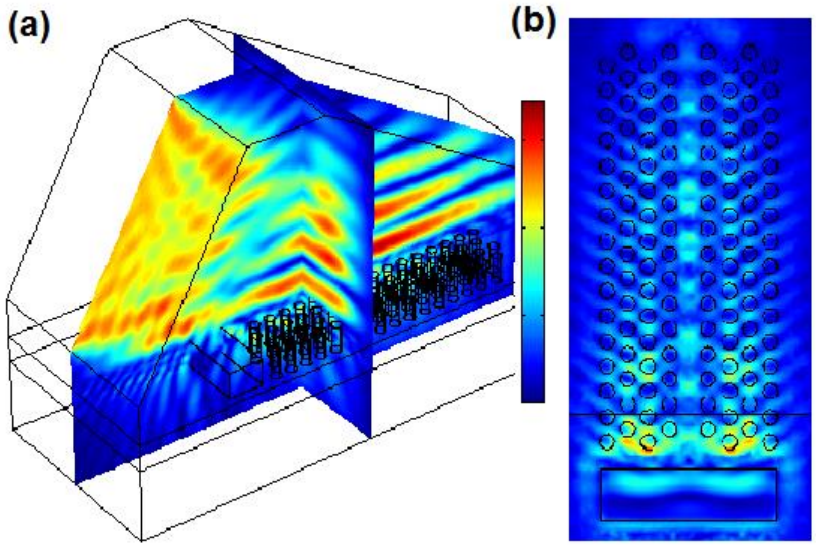

Figure 3.2: (a) Overview of the basic geometry of the COMSOL simulation geometry. The simulation replicates the experimental set up with an electric field incident on the sample at an angle of 60°. (b) Normalized electric field at the top surface of the ITO layer. It is assumed the rate of photoemission in PEEM is proportional to the square of the normalized electromagnetic field strength in COMSOL.

The evaluation is sensitive to a number of parameters such as the waveguide thickness, refractive index of ITO, the precise laser wavelength, the geometry of the air holes, particularly the holes precise shape and radius, their tapering and how far the holes extend into the glass substrate. COMSOL allows us to easily modify these parameters to see how the waveguide modes are affected. As with the slab waveguide, a line graph of

the square of the normalized electromagnetic field at the ITO surface is taken at the top ITO surface along the defect channel to approximate the photoemission in PEEM.

3.3 MEEP

Band diagrams for photonic crystal structures were calculated using a free open source Finite-Difference Time-Domain (FDTD) program called MEEP for modeling computational electrodynamics. MEEP simulates Maxwell's equations over a finite rectangular grid known as a Yee lattice. The model alternates updates between the E-field and B-field each time step across the lattice points since the E-field depends on the time derivative of the B-field and the B-field depends on the time derivative of the E-field. By defining the photonic crystal lattice geometry we can solve for the eigenmodes in the irreducible Brillouin zone (discussed further in section 4.2) which will fully describe the solutions of the photonic crystal lattice due to its periodic nature. The band diagram produced describes the allowed propagation of frequencies of light within the photonic crystal.

3.4 Localized Surface Plasmons

There are significant challenges in calculating modes of metallic particles on substrates. Mie theory is very popular for modeling optical properties of spherical particles and is valid for particles that are large enough to ignore quantum effects. While it has had much success and even been extended from Mie's original homogenous media solution to model particles on substrates [52], the implementation breaks down

when coupling between the LSPs in adjacent particles produce electromagnetic hot spots [53]–[55] and thus Mie theory is not appropriate for dealing with interacting multiparticle plasmonic systems. Another popular method is the Discrete Dipole Approximation (DDA) which has been shown to accurately predict plasmonic resonances of spheres and sphere clusters. The asymmetry due to the introduction of a substrate causes inaccuracies where the DDA appears to overestimate the size of the particle [56]. There are several corrections available to account for the substrate effects on a single particle or the dipolar interaction [57]–[59], but it is unclear how these perform when also accounting for both substrate and interparticle interaction. Finite Element Method has been shown to be a valid, though computationally expensive, for calculating plasmonic modes of complicated asymmetric geometries [60]. In our work we use a commercially available FEM modeling program, COMSOL, to simulate the plasmonic responses of dimers mediated by metallic and dielectric substrates. We limit ourselves to the regime where the spacing between the particle is greater than 0.5nm as smaller spaces give rise to quantum tunneling effects[61] which are not accounted for in FEM modeling.

A tetrahedral mesh is defined over the sample geometry. There is a minimum element size of one tenth of the wavelength with the spheres having a finer resolution of 2nm. The material parameters are defined in terms of the refractive index using Johnson and Christie [62] for silver and gold, a refractive index of 2.1 for the ITO layer. A cylindrical symmetry with a scattering boundary condition is used for the simulation boundary as depicted in Figure 3.3. While the scattering boundary produces some back

reflection, the plasmonic response of the nanoparticles is orders of magnitude greater allowing us to reasonably ignore any errors from imperfect boundary conditions. The electric field is defined at one boundary of the simulation approximating the incident light in the experiment. The square of the normalized electric field from the surface of the nanoparticles is exported, the photoelectron yield observed in N-PEEM is a corresponds this parameter to the m_{th} power where m is the number of photons required to produce a single photoelectron.

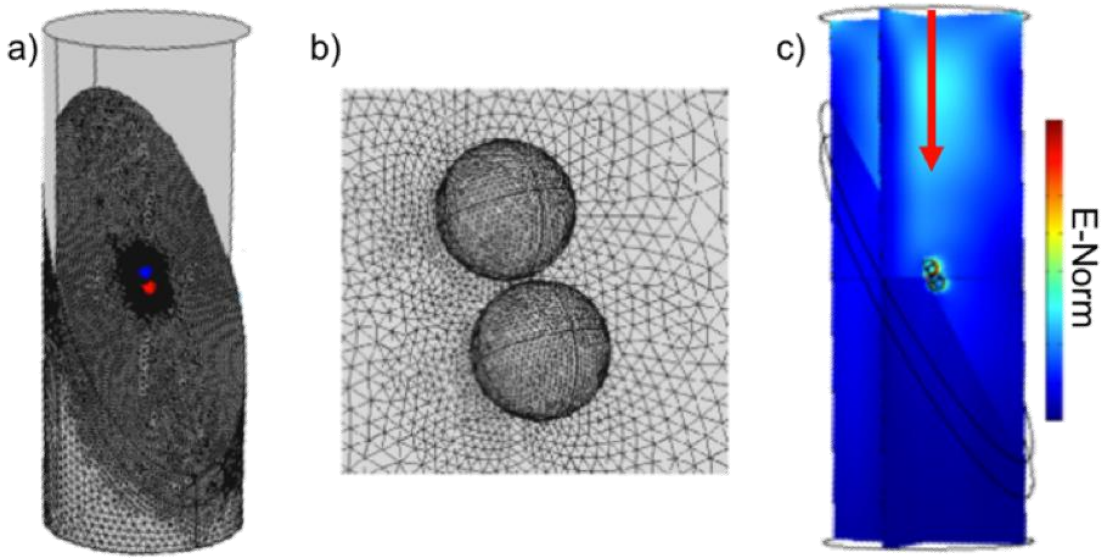

Figure 3.3: a) An overview of the simulation geometry. The spheres are highlighted in red and blue to distinguish them from the substrate. b) Close up of the spheres. c) The electric field is defined at the top surface and propagates downwards exciting the plasmonic response in the silver nanospheres.

The nanosphere dimer supports several plasmonic resonances, to be discussed in more detail in section 5.3, which correspond to an increase in E_{norm} at the surface of the nanoparticles when excited. The wavelength at which they occur and the relative strength of the various resonances are determined by fitting the simulated data to a

series of gaussians using a regression analysis as in Figure 3.4. The simulations allow us to extend the wavelength sweep beyond the available laser spectrum in experimentation and thus there are three expected modes which we define as the transverse single sphere mode, the longitudinal dimer mode, and the longitudinal single sphere mode. The longitudinal single sphere mode is at a wavelength below the available range of our laser and thus can only be determined in simulation.

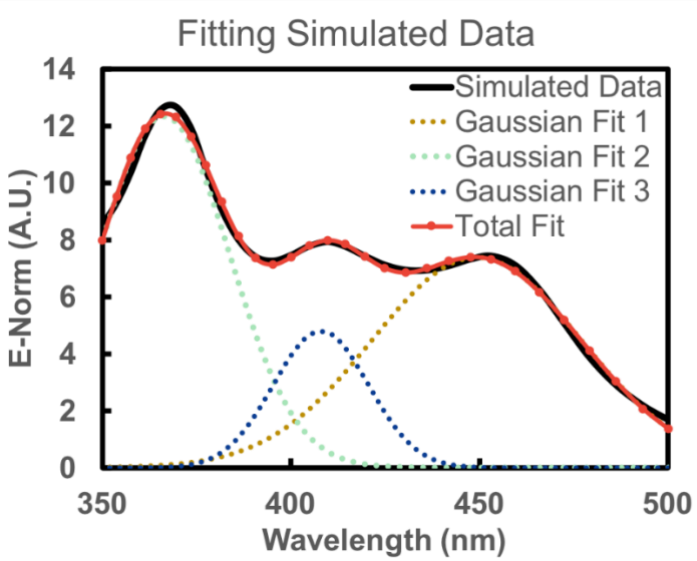

Figure 3.4: Fitting of the simulated data of a dimer on an ITO substrate to determine the resonances in the dipole. Three gaussians are used to account for the three main expected modes, the transverse single sphere mode (light green), the longitudinal dipolar mode (blue), and the longitudinal single sphere mode (dark yellow).

4 Photonics in PEEM

Results presented in this chapter have previously been published in

T. Stenmark, R. C. Word, and R. Könenkamp, "Confined photonic mode propagation observed in photoemission electron microscopy," *Ultramicroscopy*, vol. 183, 2017, doi: 10.1016/j.ultramic.2017.06.013.

T. Stenmark and R. Könenkamp, "Photoemission electron microscopy to characterize slow light in a photonic crystal line defect," *Phys. Rev. B*, vol. 99, no. 20, 2019, doi: 10.1103/PhysRevB.99.205428.

4.1 Photonic Slab Waveguide Modes

In order for a mode to propagate in a thin film waveguide, the mode must fulfill the transverse resonance condition, that is the phase undergone in a round trip from one interface and back plus the Fresnel phase shifts obtained upon reflection from the interfaces sum to an integer multiple of 2π as in eq. 4.1 ,

$$d * n * k_0 + \boldsymbol{\Phi_1} + \boldsymbol{\Phi_2} = m * 2\pi \,, \tag{4.1}$$

where d is the distance travelled, n is the refractive index of the media, k_0 is the free space wavenumber, $\boldsymbol{\Phi}_1$ and $\boldsymbol{\Phi}_2$ are the Fresnel phase shifts from the two interfaces, and m is an integer. If this condition is not met, the mode will self-interfere and be damped out [63]. The light coupling into the waveguide by diffracting off the edge of the trench that fulfills the resonance condition will be allowed to propagate through the ITO while forbidden modes will not.

For our specific waveguide parameters the resonance condition allows two TE polarized modes to propagate in the ITO layer and in order to characterize these modes we use an

interferometric approach. The incident laser pulse that excites the guided modes will also interfere with the guided modes creating a standing interference pattern. Because images in PEEM are time averaged images of the photoemission yield, only stationary patterns will be distinguishable in the image as propagating waves do not give rise to contrast in time averaged images. The stationary areas of constructive interference produce more electron emission and show up as a bright area in PEEM, while dark areas correspond to destructive interference as for example in Figure 4.1.

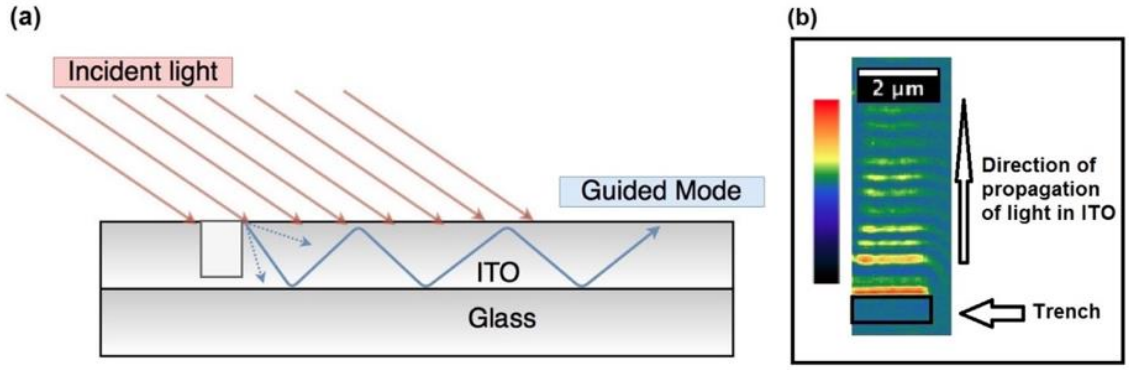

Figure 4.1: (a) schematic of light diffracting off of the trench edge into the ITO layer. (b) PEEM image of interference pattern created by coupled modes and incident light.

To determine the spacing of the fringes in the standing interference pattern we take the laterally averaged pixel intensity from the PEEM image in the direction of propagation and take the Fourier transform of the resulting line graph as in Figure 4.2. The frequency of the pattern divided by the sampling distance produces a periodogram, as seen in Figure 4.2c, with peaks labeled 1 and 2 corresponding to the primary allowed modes. Additional features appear in the periodogram as well. The peak labeled 5 corresponds to the beating pattern between the two main modes, while the peak labeled 3 correspond to a mode that is near the cut off frequency of the waveguide. This mode

only appears near the coupling trench and is damped out quickly. The small peaks labeled 4 at low periodicity are a result of the Fourier decomposition of the higher order sine function. Similarly, from COMSOL simulation a Fourier transform of the line graph of the time averaged electromagnetic field intensity at the surface ITO waveguide is taken to create a periodogram from the simulated data.

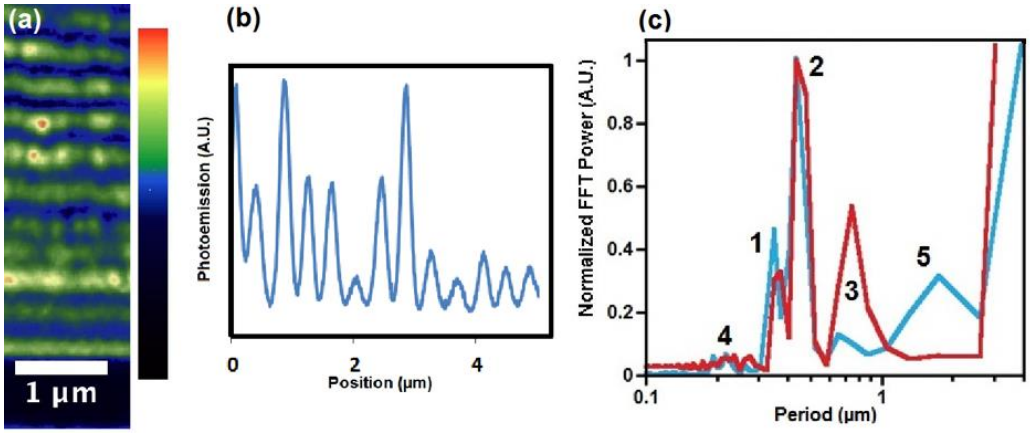

Figure 4.2: (a) Colorized PEEM image of interference pattern created by coupled modes and incident light.(b) line graph of photoemission with distance from the coupling trench. (c) Periodograms of the slab waveguide for λ=410nm showing experimental (red) and simulation (blue) results for TE polarization. Peaks 1-2 correspond to primary allowed modes. Peak 5 represents the beating pattern of modes 1 and 2. Peak 3 corresponds to a near cutoff mode that appears strongly only in the region closest to the coupling trench. The small peaks labeled 4 are produced due to the decomposition of the higher order sine function in the Fourier transform.

Once the periodicity of the interference is known we can determine the k-vector of the propagating modes using the known k-vector of the incident light and the k-vector determined by the interference spacing from the periodogram. From the k-vector of the mode we can then calculate an effective index for the guided mode. From the effective

index one can determine the speed the mode propagates in the waveguide relative to the vacuum speed of light.

$$\vec{k}_{mode} - \vec{k}_{incident} = \vec{k}_{interference}. \tag{4.2}$$

$$n_{eff} = k_{mode} \frac{\lambda_0}{2\pi}. \tag{4.3}$$

We assume that this then determines the effective index of the mode for the peak frequency of the laser pulse. Going a step further we can consider how this effective index changes with excitation frequency. This relation between the propagation of the mode and the frequency gives the group velocity. In isotropic media the group velocity of a wave packet is given by:

$$v_g = \frac{d\omega}{dk}, \tag{4.4}$$

where ω is the angular frequency and k the wavenumber. With a change of variables this may be expressed as:

$$v_g = \frac{c}{n - \lambda_0 \frac{dn}{d\lambda_0}} \tag{4.5}$$

Where $\boldsymbol{\lambda}_o$ is the free space wavelength and n is the material refractive index. Or in terms of a group index:

$$n_g = \frac{c}{v_g} = n - \lambda_0 \frac{dn}{d\lambda_0}. \tag{4.6}$$

The propagation constant of the waveguide, β, which takes into account the geometrical properties of the waveguide can be defined in terms of an effective index of the waveguide mode as

$$\beta = N_{eff} * \frac{2\pi}{\lambda_0}. \tag{4.7}$$

Taking this into account the group velocity and group index of a wave guiding structure then become:

$$v_g = \frac{d\omega}{d\beta}, \tag{4.8}$$

$$n_g = N_{eff} - \lambda_0 \frac{dN_{eff}}{d\lambda_0}. \tag{4.9}$$

By taking a series of PEEM images and tuning excitation wavelengths from 390nm-415nm we can measure the change of the effective index of the waveguide modes with respect to wavelength and by using equation 4.9 we obtain the group index of the two guided modes as seen in Figure 4.3.

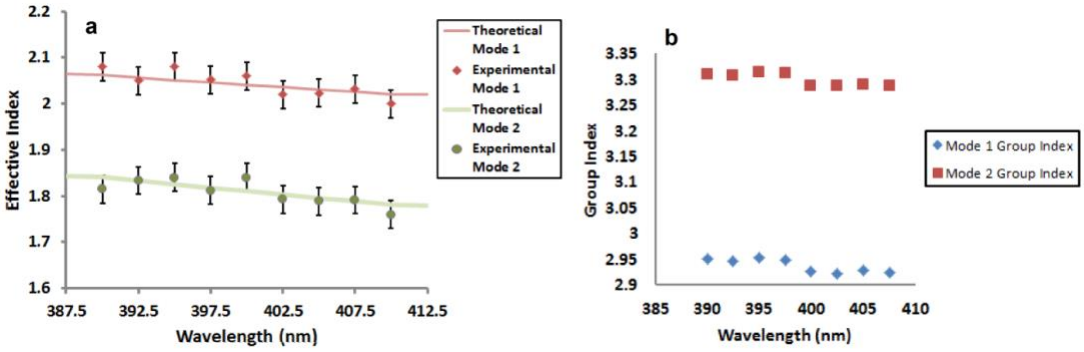

Figure 4.3: (a) Effective index vs. wavelength as measured experimentally by PEEM. Solid lines represent the theoretical relationship based on analytic solutions to the slab waveguide modes. (b) Group index of guided modes based on effective index to wavelength relation. A slight jump in the group index corresponds to a change in the refractive index of ITO's dependence on wavelength. That is $\frac{dn_{ito}}{d\lambda}$ increases just below 400nm.

The group velocity tells us how fast information can be sent through the structure and is given by the speed of light over the group index. A large group index can be useful or detrimental depending on the application. Telecommunications generally desire low group index fibers in order to maintain signal integrity and speed. The design of such

fibers is a very active area of research particularly for telecommunication bandwidths [64], [65]. Other applications such as sensing can make use of large group indexes using the increased electromagnetic field to increase sensitivity [66]. Planar slab waveguides generally do not exhibit strong slow light effects, slow light referring to light propagation that has a very large group index; however other structures, such as photonic crystal waveguides, have the ability to produce large group indexes.

4.2 Photonic Crystals

A photonic crystal is formed when there is a periodic modulation in the refractive index of a material. A common example of a one-dimensional case is a Bragg mirror which is often used to make highly reflective optical mirrors. A Bragg mirror is formed by alternating layers of dielectric material. With correctly designed thicknesses the transmitted light destructively interferes at certain wavelengths while the reflected light constructively interferes giving close to one hundred percent reflectivity for that wavelength. This is essentially a bang gap which prevents certain wavelengths from propagating through the mirror. Expanding into two dimensions, a 2D photonic crystal consists of a two-dimensional array of modulations in the refractive index. Any pattern that can be described by two basis vectors can be considered a 2D crystal configuration. The three most common configurations are square, triangular and honeycomb lattices. Similar to a Bragg mirror at certain wavelengths constructive and destructive interferences can cause near total reflection or transmission, only with the complexity of an additional dimension. Three-dimensional photonic crystals require a vertical

periodicity as well and are difficult to construct in the visible wavelength region. While several groups have created three dimensional structures for visible light [67], [68], they remain unfeasible for most applications due to the difficulty and expense of construction.

Propagation of light in a photonic crystal can be characterized in terms of a band diagram which shows the photon energy-momentum dependence for various spatial directions. Consider a triangular lattice in 2 dimensions with a constant periodicity, in reciprocal space we can consider just a single unit cell, the first Brillion zone, and within that the irreducible Brillion zone with lattice points Γ, M, K as seen in Figure 4.4. Any k-vector in reciprocal space can be projected into the irreducible Brillion zone by argument of symmetry. Linearly polarized light can be broken into two polarization components, transverse electric (TE) with the electric field in the plane of periodicity and transverse magnetic (TM) with the magnetic field in the plane of periodicity. Calculating band diagrams generally requires computational software. For our calculation we use MEEP which takes a Finite-Difference Time-Domain (FDTD) approach to compute band diagrams of photonic crystal structures.

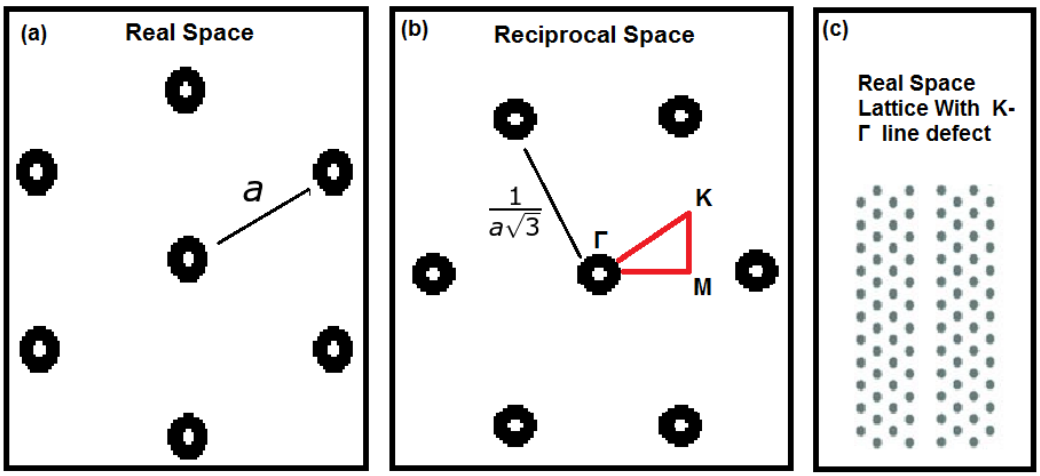

Figure 4.4: Triangular lattice in (a) real space with a periodicity of a (b) in reciprocal space. The irreducible Brillion zone is indicated by points labeled Γ, M, K. Any lattice vector can be projected into the irreducible Brillion by symmetry. (c) Real space triangular lattice with a line defect in the K- Γ direction.

It is standard to normalize the frequency to the real space periodicity of the photonic crystal. Thus we will be representing the frequency in band diagrams as the angular frequency of the light divided by the spatial angular frequency of the periodicity of the lattice, $\frac{\omega a}{2\pi c}$, which can then be simplified to $\frac{a}{\lambda}$, where λ is the free space wavelength. Similarly, the photon k-vector in the crystal is normalized to the k-vector of the periodicity, $k\frac{a}{2\pi}$For certain values of k and ω the band diagram will exhibit a band gap, a range of frequencies for which propagation is forbidden in all directions in the photonic crystal. A band diagram for a true 2D case with a triangular lattice of air holes in ITO with a hole-radius of 0.35 times the periodicity for TE modes can be seen in Figure 4.5.

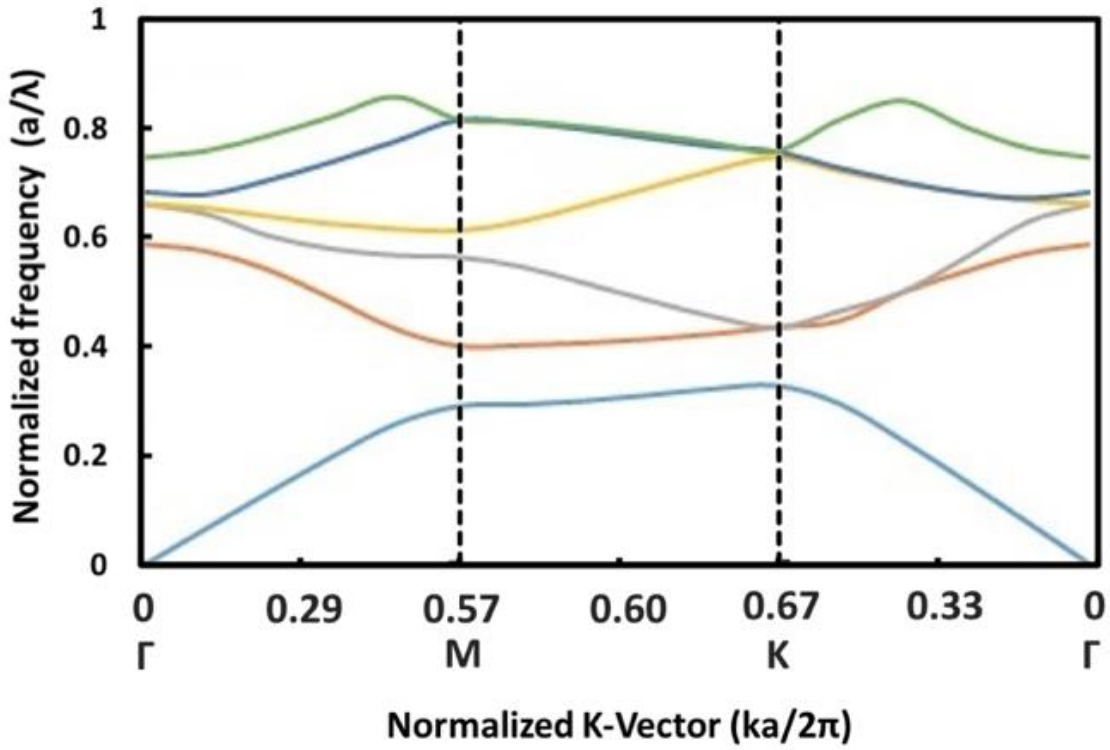

Figure 4.5: Band diagram for 2D triangular air hole lattice with radius of 0.35*a in ITO for TE polarization calculated with MEEP. A band gap exists for normalized frequencies from ~0.36-0.42

By leaving a single row of holes out of the photonic crystal pattern, as in Figure 4.4c, a line defect is created that acts a waveguide. The mode can be confined to the channel both by the band gap effects and refractive index contrast mechanisms. This mode is capable of producing a very small group velocity when the frequency approaches the edge of the band gap, $E_G/\hbar$, where E_G is the band gap of the photonic crystal. As the mode approaches the band edge, the defect mode may couple to the propagating modes of the crystal. This occurs when the k-vector of the defect mode matches the k-vector at the band edge. Since the $\omega(k)$ is relatively flat at the band edge, a small

change in frequency produces a large change in k-vector which per equation 4.4 indicating a small group velocity.

Unfortunately, 2D structures are not physically realizable for dielectric materials and 3D structures present extreme fabrication challenges. A more achievable geometry is to use a photonic crystal slab, this is the case where a thin dielectric waveguide has a periodicity introduced in two dimensions in the xy-plane while the light is confined in the z direction via total internal reflection. A photonic crystal slab that has symmetry in the z direction, with the same material for substrate and superstrate, can have its modes broken into TE-like and TM-like modes. The TE, TM designation refers to the dominant orientation of the electromagnetic field in the slab, where TE-like modes have the electric field of the confined mode aligned more parallel to the interface and TM-like modes have the electric field aligned more perpendicular to the interface.

In many cases a symmetric cladding is not easy to engineer, and it is much simpler to have the PC resting on a substrate with air or vacuum above. In this case the symmetry is broken and the TE-like and TM-like modes are able to couple with each other. This means a waveguide where a complete band gap exists for only one mode type will become leaky as the coupled light radiates away [69]. Additionally the introduction of a substrate tends to pull bands down to lower frequencies, reducing or destroying the band gap [70]. Such structures can still display interesting properties, such as slow light, even without a complete band gap but tend to be lossy.

The defect mode in a photonic crystal slab is similar to that of a rectangular waveguide being confined in the vertical direction by the refractive index and prevented from radiating into the photonic crystal by Bragg-like reflections from the periodic array of holes as well as refractive index contrast. Figure 4.6 shows the MEEP simulation result for the band structure of such an arrangement. While we can see from the band diagram that the band gap has disappeared due to the introduction of the asymmetric slab, the defect mode can still interact with the band structure of the photonic crystal, particularly where bands flatten out and have a degree of separation for a certain range of k-vectors.

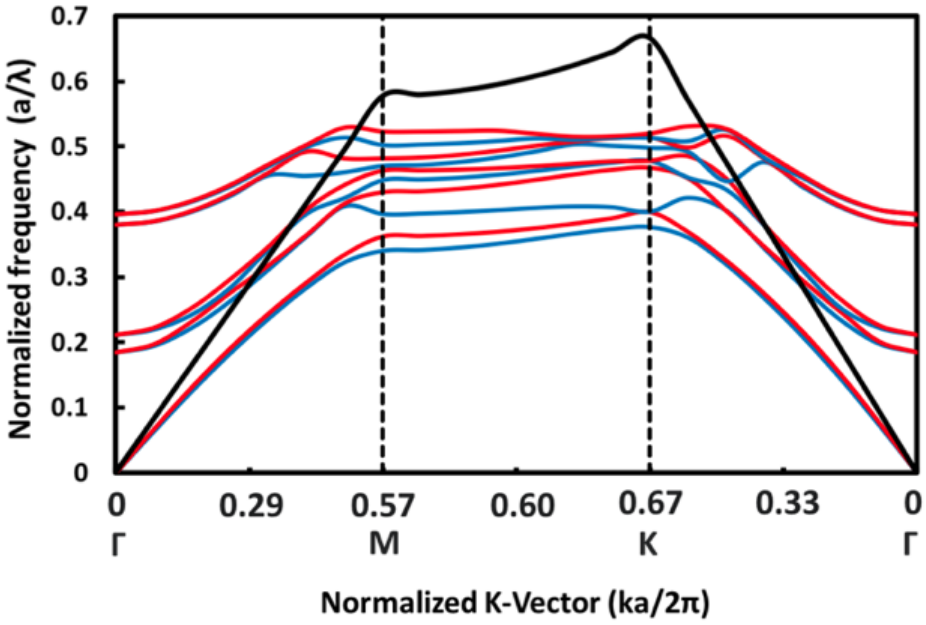

Figure 4.6: Band diagram for 2D triangular air hole lattice in a 270nm thick asymmetric slab waveguide with radius of 0.35a in ITO on glass extending infinitely in the xy plane calculated with MEEP. Red lines are TE-like modes and blue line are TM-like modes. The solid black line represents the light cone. Note the band gap at normalized frequency of ~0.4 has disappeared due to the asymmetry produced by the introduction of a substrate.

4.3 Photonic Crystal Defect Waveguide in PEEM

To evaluate the modes in the PC defect we use the same interferometric approach as taken with the slab wave guide in section 4.1. A laser pulse is incident on the coupling trench allowing light to couple into the PC defect via diffraction. The interference pattern is evaluated via Fourier transform as shown in Figure 4.7 to determine the k-vector in the K- Γ direction, and an effective index of the structure is determined as in equation 4.3. A series of images was taken at wavelengths in the range 390nm<λ<410nm with step size between 0.5 and 1nm to determine the dependence of effective index on wavelength.

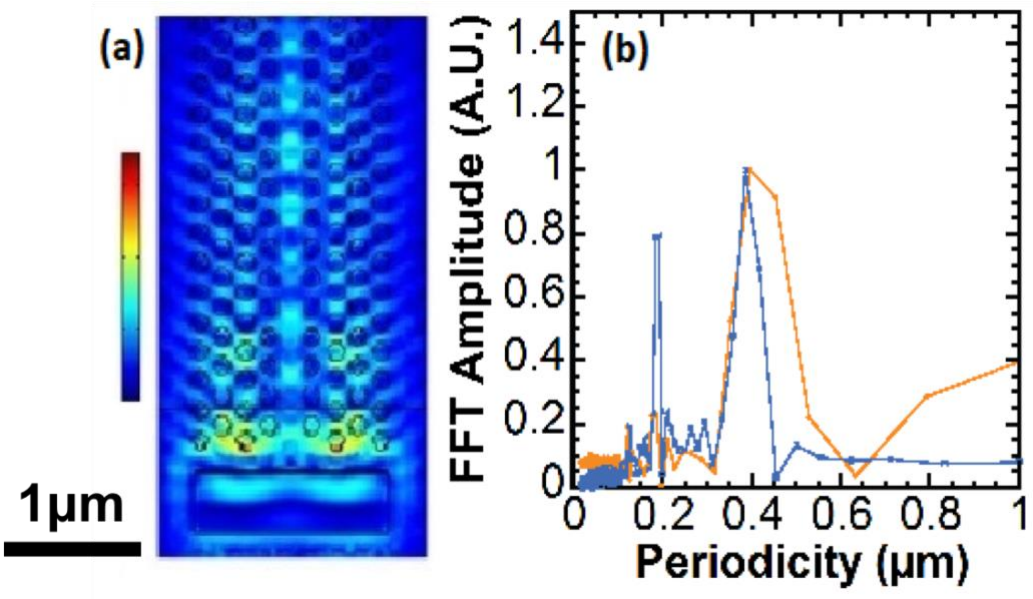

Figure 4.7: (a) Time-averaged normalized E-field distribution at the ITO surface obtained from the numerical simulation with a wavelength of 400nm. (b) A comparison the FFT obtained from this simulation (blue line) and an FFT obtained experimentally from PEEM image (orange line). The peak at 180nm is due to the PC hole periodicity and is more prominent in the simulated data.

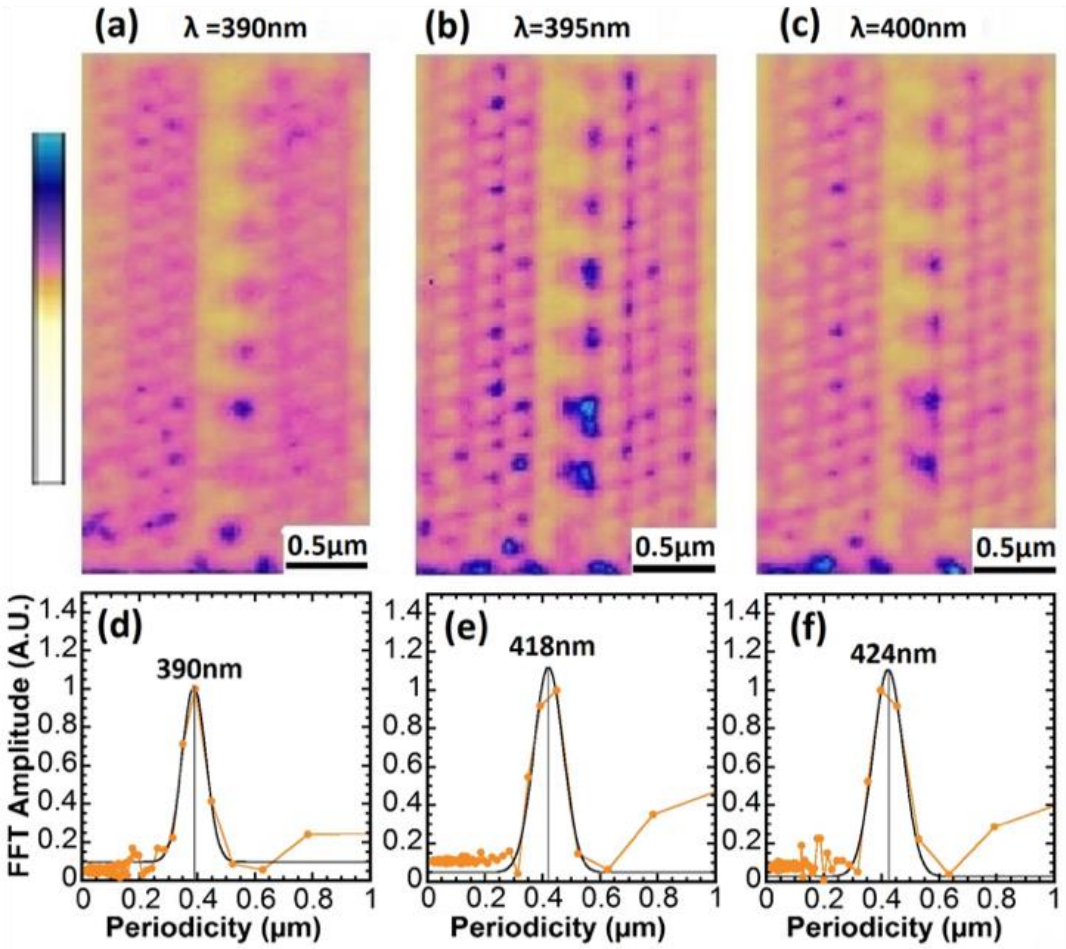

Figure 4.8: (a-c) Colorized PEEM images and accompanying periodograms at laser wavelengths of 390nm, 395nm, and 400nm, respectively. (d-f) FFT of the pixel intensity along the defect channel. A gaussian fit is used to determine the peak in the FFT spectrum. (g) A simulation of the waveguide at 400nm illumination.

By selecting reasonable choices for simulation parameters for ITO thickness, hole radius, and depth of hole into the glass within the uncertainties of the sample geometry, we were able to obtain excellent agreement between experimental and simulated results. The parameters for two simulated results displayed in Figure 4.9 are laid out in Table 4-1. These two particular sets of parameters are chosen to highlight how parameter

changes within our experimental uncertainty can significantly change the effective index vs. wavelength relationship and the magnitude of the slow light effect.

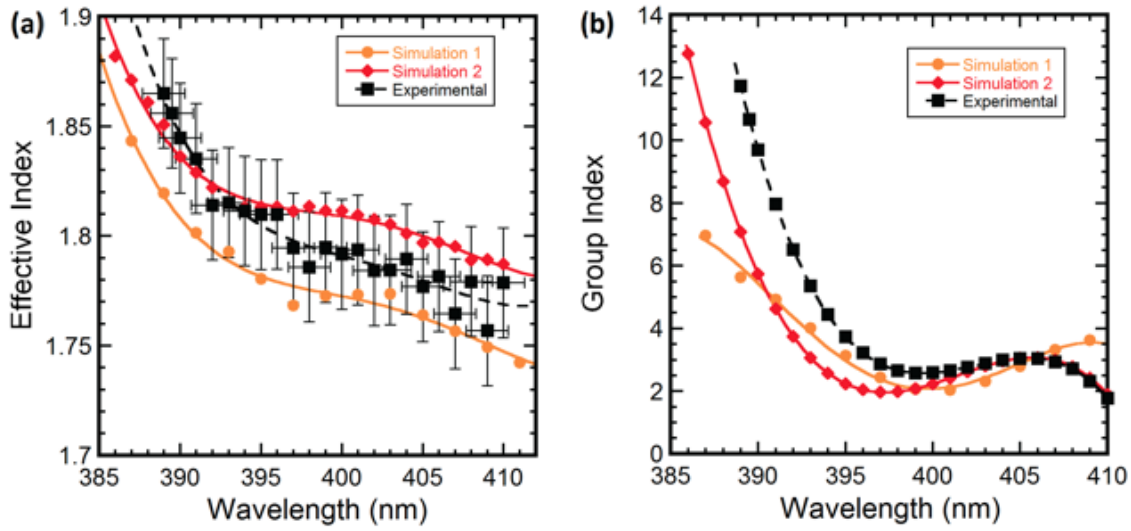

Figure 4.9: (a) Experimental and calculated results for the effective index vs. wavelength for the defect mode of the photonic waveguide. The difference in parameters between the two sets of calculated data are given in Table 4-1. (b) Experimental and calculated group index vs. wavelength obtained from eq. (4.9) and a polynomial least-square fit for the effective index data in part (a) of the figure. The parameters used for the two simulation models are listed in Table 4-1.

	ITO Thickness	Hole Radius	Depth into Glass
Simulation 1	280nm	45nm	0nm
Simulation 2	260nm	50nm	90nm

Table 4-1*: List of parameters varied between simulations.*

From both the experimental and simulated results we determine a sharp increase in the effective index and thus a slowdown of the group velocity in the wavelength region below 395nm. These results can be rationalized by looking at the band diagram in this

region. Projecting the experimentally obtained dispersion curve onto the PC band diagram we then find that the dispersion curve for the channel mode flattens near a/λ = 0.5 as indicated in Figure 4.10. This corresponds to the edge of the Brillouin zone for the line defect [71], [72] and indicates that the observed slowdown is due to interaction with the periodic structure of the waveguide.

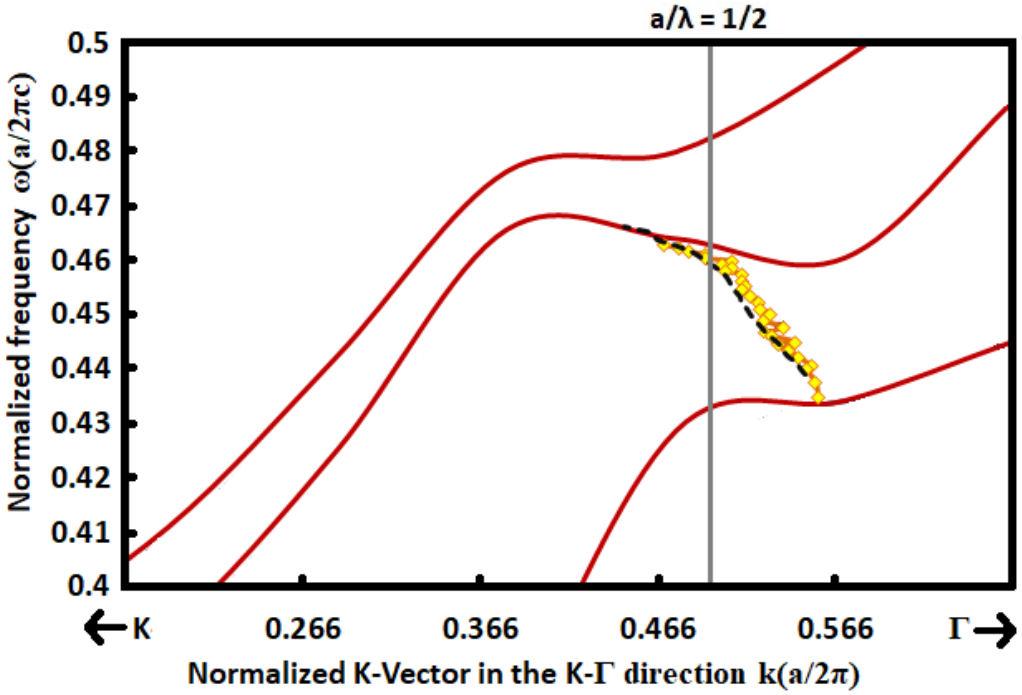

Figure 4.10: Band diagram in the Γ→K direction of TE like modes calculated with MEEP for a PC with parameters corresponding to Simulation 2. Yellow dots represent the experimentally determined k-vector of the guided mode in the Γ→K direction projected on the first Brillouin zone. The dashed black line shows the k-vector obtained in Simulation-2. A vertical line marks a/λ = 0.5 which corresponds to the projected Brillouin zone edge for the defect waveguide.

Furthermore, we find that the dispersion curve of the line-defect mode closely approaches a TE-like band and bends to follow the band structure indicating a coupling of the guided to the PC band structure and a further decrease of the group velocity as a consequence of the shape of the band structure. Both effects, the proximity to the line-

defect Brillouin zone boundary as well as the approach of the line-defect dispersion curve towards a flat TE-like band in the photonic crystal may therefore contribute to the observed slow light effects.

5 Plasmonics in PEEM

5.1 Introduction to Plasmonics

Localized surface plasmons (LSP) have attracted significant attention from researchers due to their ability to confine light past the optical diffraction limit [73]. A plasmon is generally defined as the oscillation of the electron density in a material. The energy of the plasmon, $\mathrm{E_P}$, depends on the density of conduction electrons, *n*. A plasmon can be excited with a driving force that matches the plasmon frequency, ω_p. The relationship can be approximated using a free electron model as shown in eq. 5.1 where *e* is the fundamental charge, *m* is the mass of an electron, and ϵ_0 is the permittivity of free space.

$$E_P = \hbar\sqrt{\frac{ne^2}{m\epsilon_0}} = \hbar\omega_p \tag{5.1}$$

If the plasmon occurs in a solid *m* is replaced by the effective electron mass m_e. Plasmons can be further classified based on the geometry of the system in which they occur. When the electron oscillation is throughout the material it is considered a bulk plasmon and its properties are governed by eq. 5.1. When the electron oscillation is at the interface between two materials, it is considered a surface plasmon. The combination of the charge oscillation and the electromagnetic field in the air or dielectric is termed a surface plasmon polariton (SPP) and its properties are primarily defined by the optical properties of the two materials. The surface plasmon energy is found to be

$$E_s = \frac{E_P}{\sqrt{1+\varepsilon_2}}. \tag{5.2}$$

Where ε_2 is the permittivity of the dielectric material bordering the interface of the plasmonic material, typically a metal. When the structure supporting the oscillation becomes smaller than the plasmon wavelength, the electron oscillation is considered a localized surface plasmon polariton (LSP) and its properties are defined by both the material and shape of the structure as well as the surrounding environment.

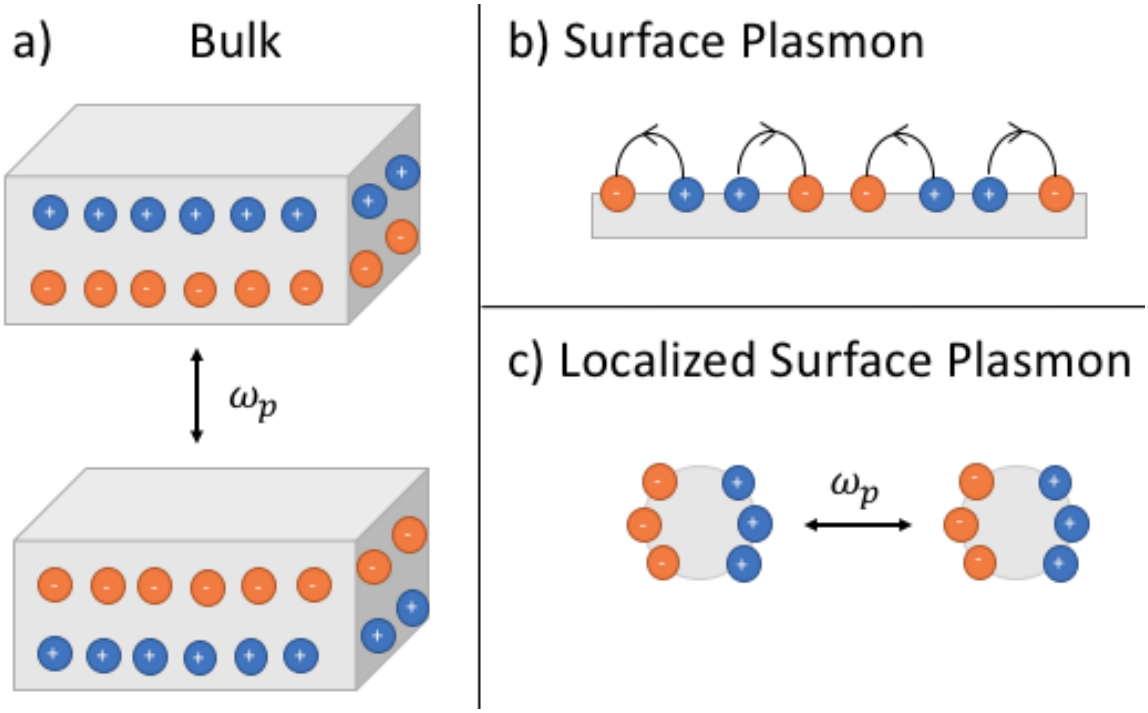

Figure 5.1: a) The bulk plasmon produced by charge oscillation throughout the bulk of the material. b) Surface plasmon polaritons produced by charge oscillation along the material surface. c) Localized Surface plasmon, charge oscillation in a structure with size comparable to the wavelength associated with the plasmon frequency.

Surface plasmons are in an intriguing area of study in PEEM due to the dependence of the rate of photoemission of electromagnetic field intensity. LSP resonances in metallic

nanoparticles (NP) have attracted considerable attention for their resonance characteristics and ability to confine electromagnetic fields in sub diffraction limit regions. They are of great use particularly in bio-sensing application [74]–[76]. Over the last two decades the synthesis [77], [78] and properties of metallic NPs have been studied extensively [79], [80]. Of great importance are both the effects of the surrounding environment as well as inter-particle resonances. Mock et al. demonstrated that a red shift occurs in the SPP resonance of an individual metallic NP as the refractive index surrounding material is increased [81] [82]. Similarly the LSP resonance of a NP resting on a dielectric substrate tends to red shift from that of the isolated NP [83]–[86]. Substrate-NP interactions are particularly pronounced when a metallic substrate is introduced. Both the separation distance of the particle from substrate and the substrate properties can be used to tune the LSP resonance [87]–[90].

The bulk properties of particles are well understood, but as we move toward nanoscale systems understanding the LSP response in individual and small groups of nanoparticles becomes critical. There are a number of interesting effects such as substrate interactions and coupling between particles which play a role in the system and must be considered to fully characterize the LSP response. There have been numerous studies of plasmonic dimers and interparticle spacing [91]–[98] but there is a gap in the literature in studies considering both interparticle coupling and the role of the substrate in the interaction, particularly when the excitation is not at normal incidence. This type of interaction is important because in applications substrates are typically needed and

normal illumination is not always practical. Additionally using oblique incidence for the incoming light provides an additional degree of freedom in illumination direction and greater control over the excitation. Developing tools and techniques, such as PEEM, to experimentally measure and model these effects is vital to actualizing future applications. We are particularly interested in observing strongly coupled systems of nanoparticles that produce avoided level crossing behavior and understanding the role of the substrate in these systems.

5.2 Strong Coupling

Strong coupling occurs when two oscillators are coupled such that the energy transfer between the two systems is greater than the energy lost to the environment. The classical example [99] is to take mechanical oscillators with masses M_1 and M_2 attached to two springs with spring constants K_1 and K_2. Individually each would oscillate at the frequency of,

$$\omega_n = \sqrt{\frac{K_n}{M_n}} \ , \tag{5.2}$$

With the introduction of some coupling constant, g, classically represented by a spring between the two oscillators for example, the equations of motion for two oscillators become:

$$\mathrm{M}_1 \frac{d^2}{dx^2} X_1 + K_1 X_1 + g(X_1 - X_2) = 0 \ , \tag{5.3}$$

$$\mathrm{M}_2 \frac{d^2}{dx^2} X_2 + K_2 X_2 - g(X_1 - X_2) = 0 \ , \tag{5.4}$$

Solving for the eigenfrequencies of the system yields

$$\omega_{\pm}^2 = \frac{1}{2}[\omega_1^2 + \omega_2^2 \pm \sqrt{(\omega_1^2 - \omega_2^2)^2 + 4\Gamma^2\omega_1\omega_2}] \ , \tag{5.5}$$

$$\omega_n = \sqrt{\frac{K_n+g}{M_n}} \ , \tag{5.6}$$

$$\Gamma^2 = \frac{g^2}{M_1\omega_1 M_2\omega_2} \ , \tag{5.7}$$

What we now see is that if we take K_2 to be some spring constant K_0 and vary K_1 from K_0+ ΔK to K_o-ΔK and plot the eigenfrequencies, rather than crossing as in the uncoupled case the curves bend away from each other in what is known as avoided level crossing as seen in Figure 5.2. The gap between the two eigenfrequencies depends on the coupling constant, g, with larger constants yielding a larger splitting. The frequency of the splitting is given by,

$$\omega_+ - \omega_- = \Gamma \ . \tag{5.8}$$

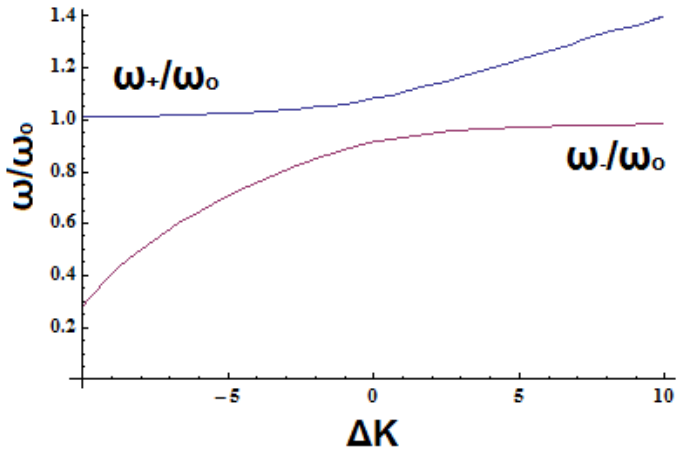

Figure 5.2: Eigenfrequencies of a system of coupled oscillators with K_2=10, K_1=10+ΔK, M_1=M_2=1, g=1.

In order to have a more realistic system we must introduce a damping term. If the damping is stronger than the coupling the frequency splitting disappears and thus the

systems are no longer considered to be strongly coupled. Modifying our equations 5.3 and 5.4 to include damping we get:

$$\mathrm{M}_1 \frac{d^2}{dx^2} X_1 - \frac{d}{dx}\gamma_1 X_1 + K_1 X_1 + g(X_1 - X_2) = 0\,, \tag{5.9}$$

$$\mathrm{M}_2 \frac{d^2}{dx^2} X_2 - \frac{d}{dx}\gamma_2 X_2 + K_2 X_2 - g(X_1 - X_2) = 0. \tag{5.10}$$

This gives rise to imaginary components of the eigenfrequencies which gives the resonance frequency a line width. In order to observe strong coupling the separation between the eigenfrequencies must be greater than the sum of the linewidths or the two eigenfrequencies smear together, appear to meet, and no avoided level crossing will be seen. This tells us that the exchange of energy between the oscillators must be greater than the losses to the environment.

Although this model is classically derived, the phenomena of frequency splitting is the same for a non-classical system [100]. Of particular interest for PEEM are optically excited strongly coupled systems. PEEM is sensitive to both photonic and plasmonic resonances and PEEM has been used successfully to image many plasmonic and photonic phenomena including plasmonic excitations in gaps between metallic nano-structures [101] [102]. A strongly coupled photonic or plasmonic resonance occurs in a coupled resonator with high-quality confinement of electromagnetic field to which the photoemission is highly sensitive, particularly for multiphoton emission processes. PEEM has potential as a characterization tool for this type of system and recently PEEM has been used to observe strong coupling between propagating surface plasmons and

localized surface plasmon modes [103]. There is considerable space to expand in particular looking at strong coupling between LSPs taking advantage of PEEM's nearfield imaging capabilities.

One challenge is to find a system that is suitable for the limitations of our instrumentation. In particular our excitation frequencies are confined to the wavelength range available with our laser, this means we need a resonance that lies either in the 780nm-880nm range or the frequency doubled 390nm-440nm available with a harmonic doubler. Additionally, the resonances need to be narrow enough to be resolvable within this excitation spectra. Silver nanospheres fit the constraints as they are widely available and exhibit plasmonic resonances in the near ultraviolet range. Figure 5.3 shows a product infographic from Sigma-Aldrich of the extinction spectra for silver spheres submerged in an aqueous solution. The peak resonance can be selected in the range of 380nm-500nm by choosing the appropriate sphere size allowing selection of the resonant mode to fit our spectral range. Also of great importance to observe strong coupling are the ability to tune modes and couple between modes. The proximity of one nanosphere to another provides a mechanism for tuning while the breaking of the symmetry provided by the substrate facilitates the coupling of modes.

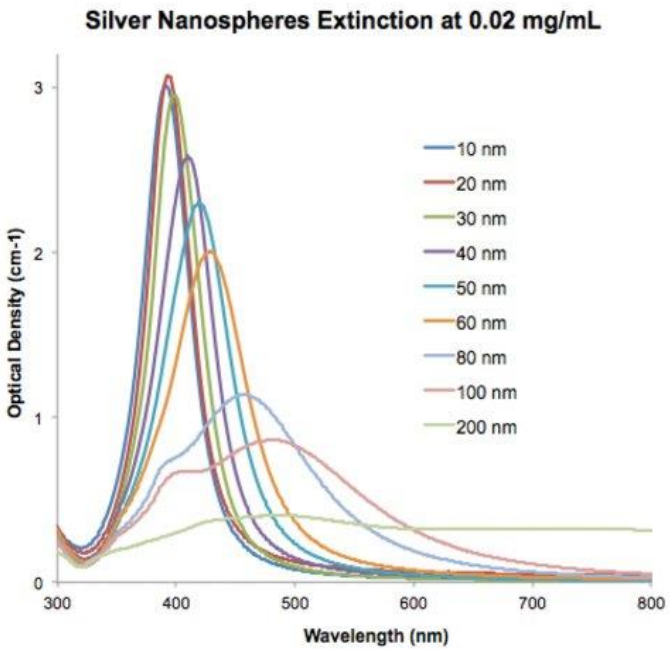

Figure 5.3: Absorption of silver nanospheres in aqueous solution with radius. Figure taken from Sigma-Aldrich product page.
https://www.sigmaaldrich.com/catalog/product/ALDRICH/730807

5.3 Plasmonic Modes in a Nanoparticle Dimer

A single metallic nanosphere will support LSP resonances, for silver nanospheres smaller than 60nm there is only a single LSP mode supported by the sphere as seen Figure 5.4.When a substrate is introduced the symmetry is broken and we can classify the resonance into two modes, one where the electric field drives the electron oscillation parallel to the substrate and one where the plasmon is driven perpendicular to the surface [104], [105]. We will classify these modes as longitudinal modes for the parallel oscillation and transverse modes for the perpendicular oscillation. The substrate effect on the longitudinal modes is very weak and only produces a slight shift in resonance

peak. The transverse modes on the other hand have a strong substrate induced red shift towards a lower energy plasmon frequency that increases with substrate index as depicted in Figure 5.4b.

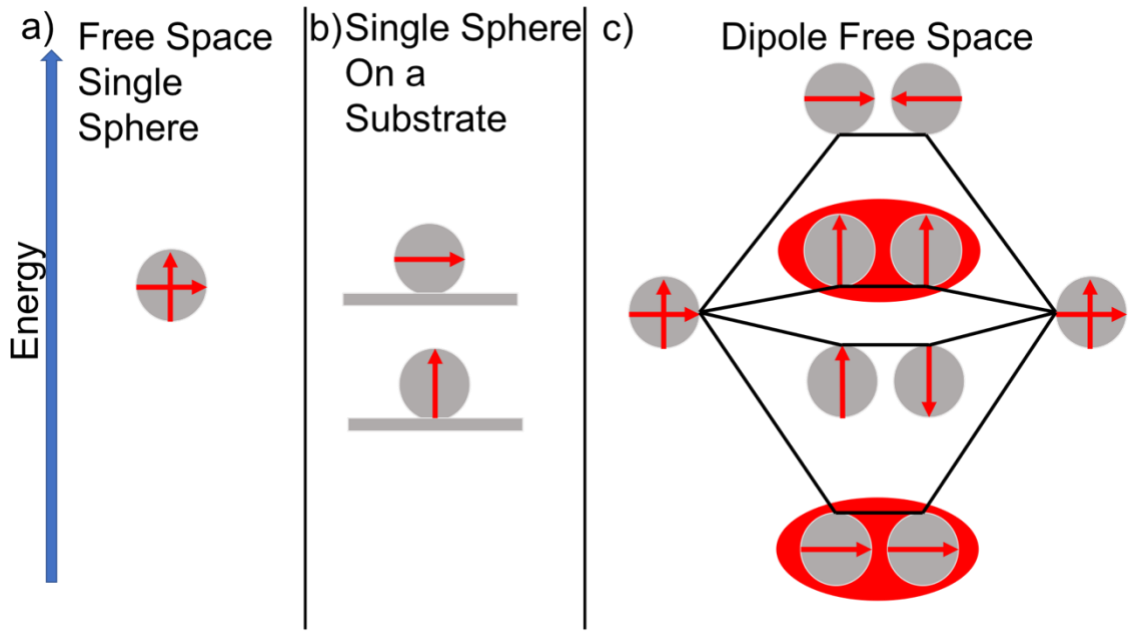

Figure 5.4: a) A single sphere in free space supports a single resonant mode, the direction of the oscillation is arbitrary due to symmetry. b) A single sphere on a substrate supports two modes, a longitudinal mode parallel to the substrate and a transverse mode perpendicular to the substrate. c) A dimer in free space has a single mode supported by each sphere and dipolar modes excited with electron oscillations on the dimer axis and off axis. The coupling between the particles is much stronger for the on-axis mode resulting in a greater shift in energy. Two of the dimer modes are bright modes highlighted in red and two are dark modes.

When a second nanoparticle is introduced to the system in addition to the modes in each individual nanoparticle there are now dimer modes. Some of these are bright dipolar modes, highlighted in red in Figure 5.4c, others are dark modes. The bright modes are radiative while dark modes are non-radiative due to having a vanishing net dipole moment and disappear in the far field. While photoemission in PEEM depends on

the nearfield and thus is capable of imaging dark modes, dark modes are not easily excited by light coupled from free space [106] which is our primary mechanism for plasmon excitation. Therefore, we will assume the primary contribution to the observed plasmonic response to be from the bright modes. The energies of the plasmon frequency of the dimer modes also depends on the separation of the spheres.

With the introduction of a substrate, the dimer modes follow a similar trend as the single sphere modes with the transverse modes red shifting while the longitudinal modes are only very weakly affected as depicted in Figure 5.5. The magnitude of the redshift depends on the refractive index of the substrate with a greater index producing a larger red shift. Because of the substrate-induced redshift of the transverse modes, there will be an energy match between the longitudinal dimer mode (LDM) and transverse single-sphere mode (TSM) at a particular sphere separation. The longitudinal and transverse modes are not strictly orthogonal due to the symmetry breaking provided by the substrate and are allowed to couple and can produce avoided level crossing. Figure 5.6 shows the response calculated in COMSOL of the modes for a dimer on a substrate as the separation between the two spheres changes. Note how the LDM approaches the TSM as the sphere separation decreases and the coupling causes the transverse single sphere mode shifts towards lower energy.

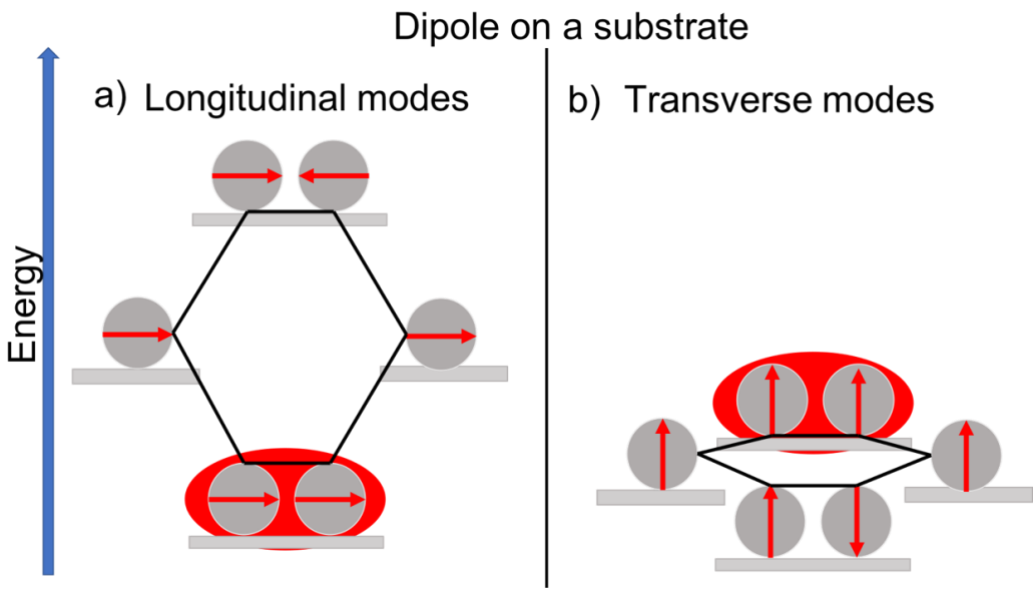

Figure 5.5: Two metallic spheres on a substrate support a) Longitudinal modes parallel to the substrate, bright mode highlighted in red. b) Red shifted transverse modes perpendicular to the substrate. The magnitude of the redshift is greater the larger the refractive index of the substrate.

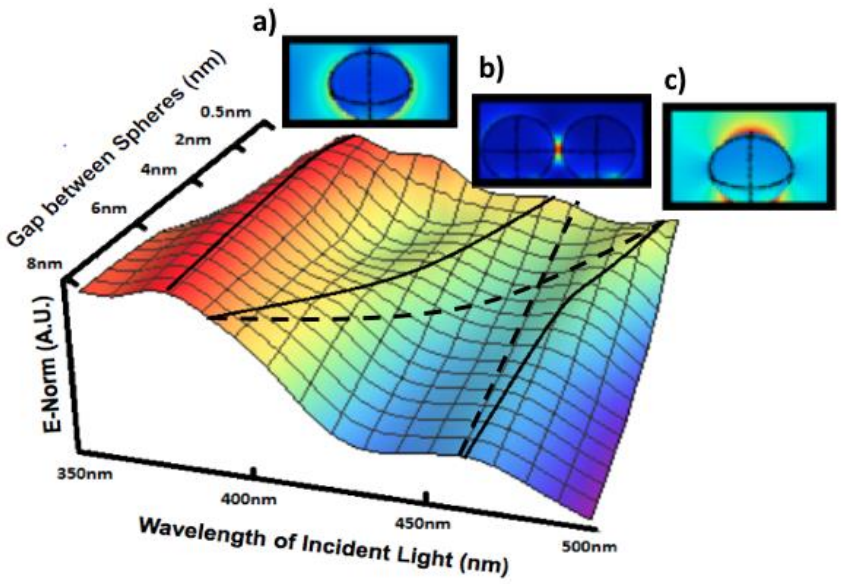

Figure 5.6: Simulated response of silver spheres on a dielectric substrate and varying gap between the spheres. Three modes are highlighted. a) The longitudinal single sphere mode. b) The longitudinal dipolar mode. c) The transverse single sphere mode. Dashed lines indicate the expected behavior of uncoupled modes

5.4 Polarization Dependence

The plasmonic response of a dimer depends on how it is excited. The polarization of the incoming light, the incident angle of the incoming light, and the direction of the incoming light with respect to the dimer axis must be considered. Here we define polarization of the incoming light with respect to the substrate, TM polarization when the magnetic field is parallel to the substrate and TE when the electric field is parallel to the substrate. For the polarization angle, ϕ, we define 0° to be TM polarization and 90° to be TE polarization. The direction of the incoming light with respect to the dimer axis designated θ as illustrated in Figure 5.7.

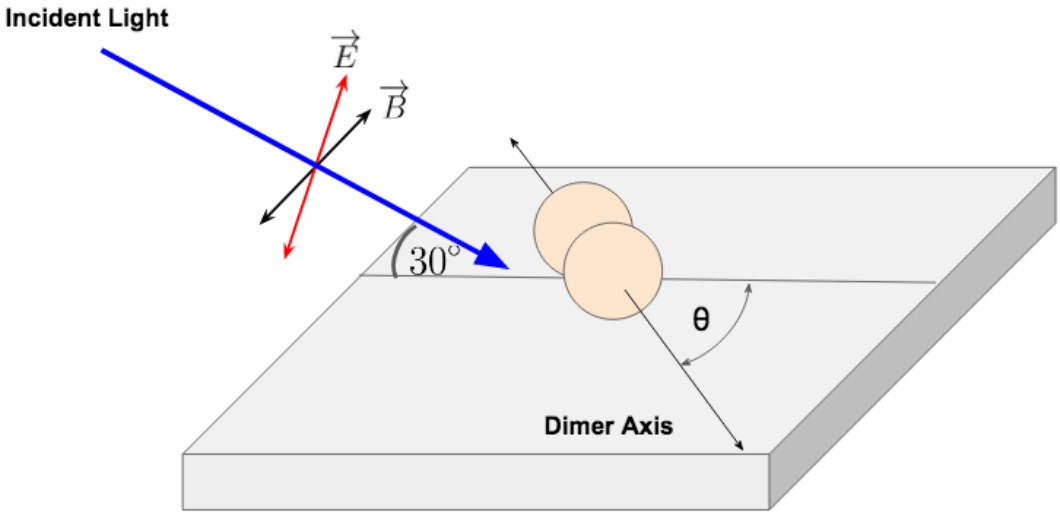

Figure 5.7: Illustration of a dipole that has an angle of θ with respect to the in plane component of the incoming light being excited by TM polarization and ϕ is the angle of the polarization with TM polarization defined as 0 degrees.

There are a number of resonant modes that can be excited in the dimer. The LDM is excited by the component of the electric field oriented along the dimer axis and the

TSM is excited by the component of the electric field aligned perpendicular to the substrate. Depending on the orientation of the dipole and polarization of the incident light these modes are excited to different degrees. The separation of the spheres also plays a role in the relative strength of the two modes. The smaller the gap between the two spheres in the dimer the stronger the LDM is in relation to the TSM.

The polarization dependence of the LDM goes as the component of E-field of the incident light aligned with the dimer axis and the polarization dependence of the TSM goes as the component of E-field of the incident light aligned with the perpendicular of the substrate. The E-field vector can be expresses as

$$E = \begin{pmatrix} 1 & 0 & 0 \\ 0 & cos(30) & -sin(30) \\ 0 & sin(30) & cos(30) \end{pmatrix} \begin{pmatrix} cos(\phi) & 0 & sin(\phi) \\ 0 & 1 & 0 \\ -sin(\phi) & 0 & cos(\phi) \end{pmatrix} \begin{pmatrix} 0 \\ 0 \\ 1 \end{pmatrix}$$

$$= \begin{pmatrix} cos(\phi) & 0 & sin(\phi) \\ sin(30)sin(\phi) & cos(30) & -sin(30)cos(\phi) \\ -cos(\phi)sin(\phi) & sin(30) & cos(30)cos(\phi) \end{pmatrix} \begin{pmatrix} 0 \\ 0 \\ 1 \end{pmatrix}$$

$$= (sin(\phi),\ -sin(30)cos(\phi),\ cos(30)cos(\phi)), \tag{5.11}$$

and the vector describing the dipole axis can be expressed as,

$$dipole\ axis = (sin(\theta),\ cos(\theta),\ 0). \tag{5.12}$$

Then the component of the E-field perpendicular to the substrate and the component aligned with the dipole axis can be expressed as

$$E_{TSM} = cos(30°)cos(\phi), \tag{5.13}$$

$$E_{LDM} = sin(\phi)sin(\theta) - sin(30)cos(\phi)cos(\theta)$$

$$= cos(\phi + \theta) + 0.5\, cos(\phi)cos(\theta). \tag{5.14}$$

The sum of the polarization dependent responses of these two modes can be modeled as the sum of the square of the two sinusoidal functions weighted by the relative strength of the two modes,

$$A(E_{TSM})^2 + B(E_{LDM})^2 . \quad (5.15)$$

The amplitudes A and B represent the relative strength of the two modes.

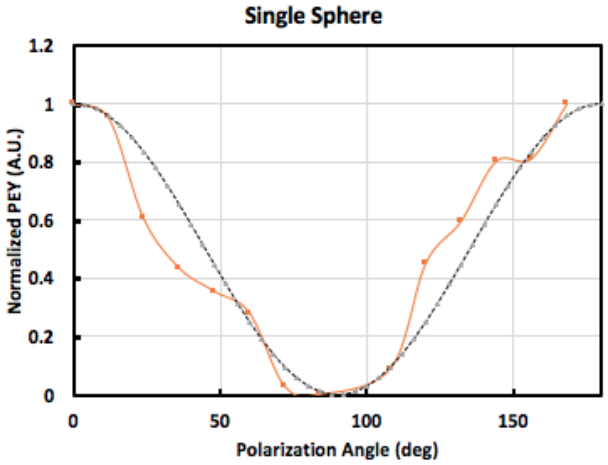

Figure 5.8: A single sphere response is given by a $\cos^2\phi$, where ϕ is the angle of the polarization. TM polarization is at 0 degrees while TE polarization is at 90 degrees. The experimental data is in orange while the fit is the dashed black line.

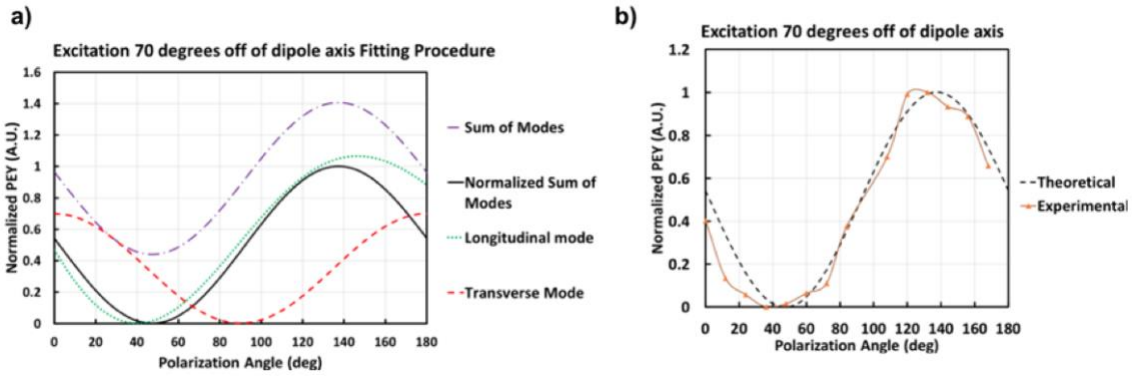

Figure 5.9: A demonstration of how the theoretical responses of the two modes are used to produce the total theoretical spectra. a) The expected response of the transverse mode (red) and longitudinal mode (green) are plotted for a dimer with an axis angle θ=70°. The sum of the modes (dashed purple) is then normalized (solid black). B) The normalized theoretical response after background subtraction (Black dashed) is compared to the experimental data (orange triangles).

For a single sphere we then expect the response to follow a simple cosine squared dependence as seen in Figure 5.8**.** For a dimer the theoretical response is calculated as demonstrated in Figure 5.9a. The polarization dependent response of the longitudinal dimer mode and transverse single sphere mode are summed, the relative amplitudes of the modes are determined from the relative amplitudes of the fitted simulated modes at the excitation wavelength of 420nm. The constant background is subtracted from the sum of the modes and then normalized. This procedure then allows comparison to the experimental data. The experimental data already consists of a sum of modes, so we simply subtract the background and normalize to one as seen in Figure 5.9b. The responses for dipoles at several different angles, θ, with respect to the incident exciting light are displayed in Figure 5.10.

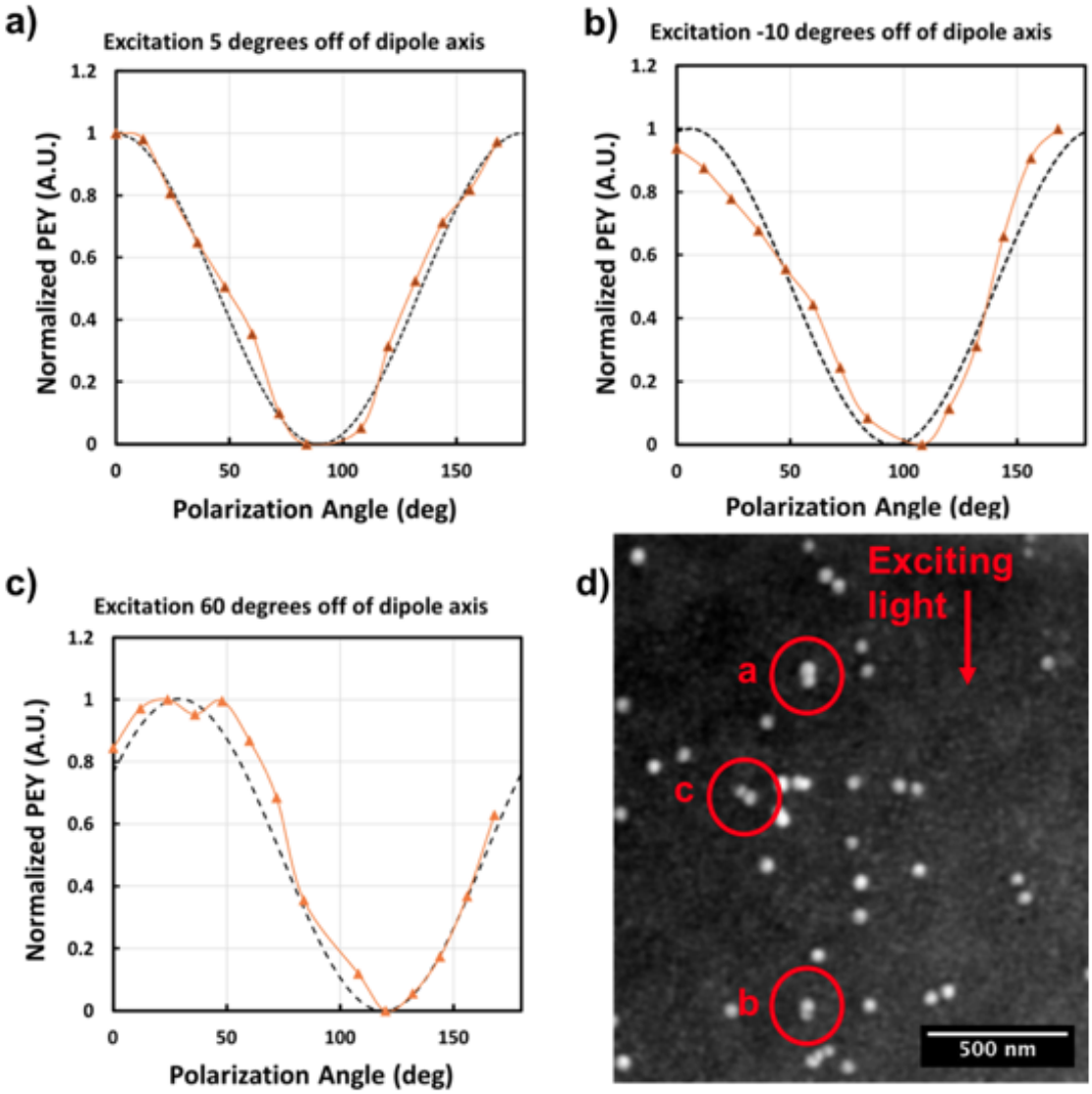

Figure 5.10: Additional examples of dipole with differing degrees, θ, of rotation from the excitation axis. TM polarization is at 0 degrees while TE polarization is at 90 degrees. Black dashed lines represent the theoretical response while orange lines represent experimental data. d) An SEM image highlighting the dipoles the experimental data comes from. The exciting light is incident from the top.

These results demonstrate the excited plasmonic resonances in a nanosphere dimer depend on the angel of incidence of the incoming light, the relative angle between the incident light and dimer axis, as well as the polarization. The excited plasmonic modes

are measurable in PEEM and can be controlled through changes in the incident angle and polarization.

5.5 Strong Coupling Observed in PEEM

In order to experimentally observe strong coupling, it is required to have two resonances one of which can be modified such that its energy is swept through a range matching the energy of the other mode at some point. For a dipole on a substrate the TSM is a constant while the LDM can be controlled by varying the separation of the spheres. As the separation between the spheres decreases, the longitudinal dipole mode is red shifted to lower energies. Depending on the substrate properties and sphere sizes at a particular separation the energy of the LDM will match the TSM. Coupling is allowed between the modes as the broken symmetry provided by the substrate breaks the orthogonality of the modes. As the energies of the modes approach each other, the coupling produces avoided level-crossing indicating a strong coupling between the modes.

Figure 5.11a shows the theoretical uncoupled behavior of the two modes for a 45nm sphere on a substrate with a refractive index 2.2. Note the intersection of the uncoupled modes at a sphere separation of ~1.6nm. Figure 5.11b demonstrates the splitting of the TSM and LDM, the modes have similar resonances when uncoupled and produce two shifted modes when allowed to interact due to the substrate mediation. While we are

unable to modify an individual dimer's separation in our experiment, we are able to identify different dimers with a range of sphere separations.

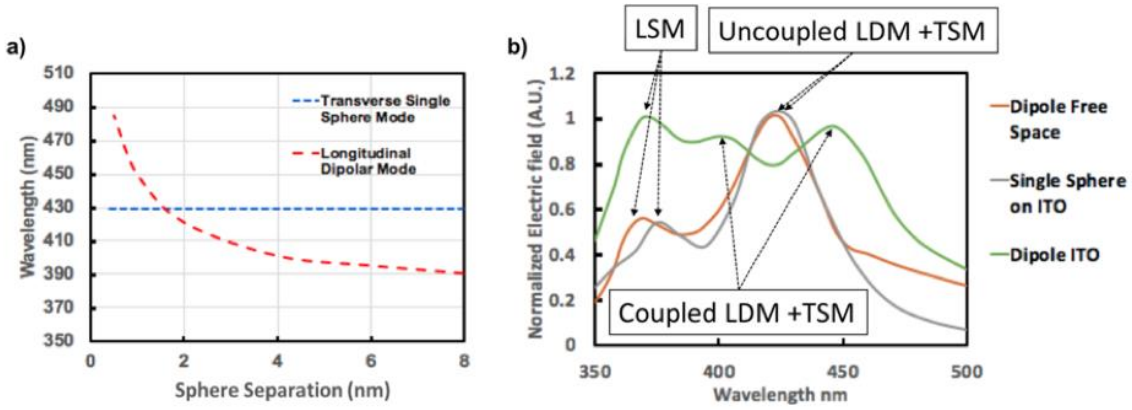

Figure 5.11: a) Simulated transverse single sphere mode and longitudinal dipole mode with no coupling. Sphere size 45nm on a substrate with refractive index of 2.2. b) Comparison of the spectral response for a dipole in free space, single sphere on ITO, and dipole on ITO. The Longitudinal single sphere mode (LSM), Longitudinal dipolar mode (LDM) and Transverse single sphere mode (TSM) are labeled.

One of the experimental challenges is the nonuniformity of the sizes of spheres. The purchased silver spheres have an average sphere diameter of 42nm with a standard deviation of 2.5nm producing a range of sphere sizes in the deposition. In order to compare the dipolar responses of different dimers of varying separation, we must be able to account for the effect of size variation on the plasmonic response. An increased sphere size corresponds to both a redshifted TSM and a redshifted LDM. The separation that produces an energy match between the two modes stays very nearly the same for dipolar pairs of different sizes as seen from the simulated data in Figure 5.12.

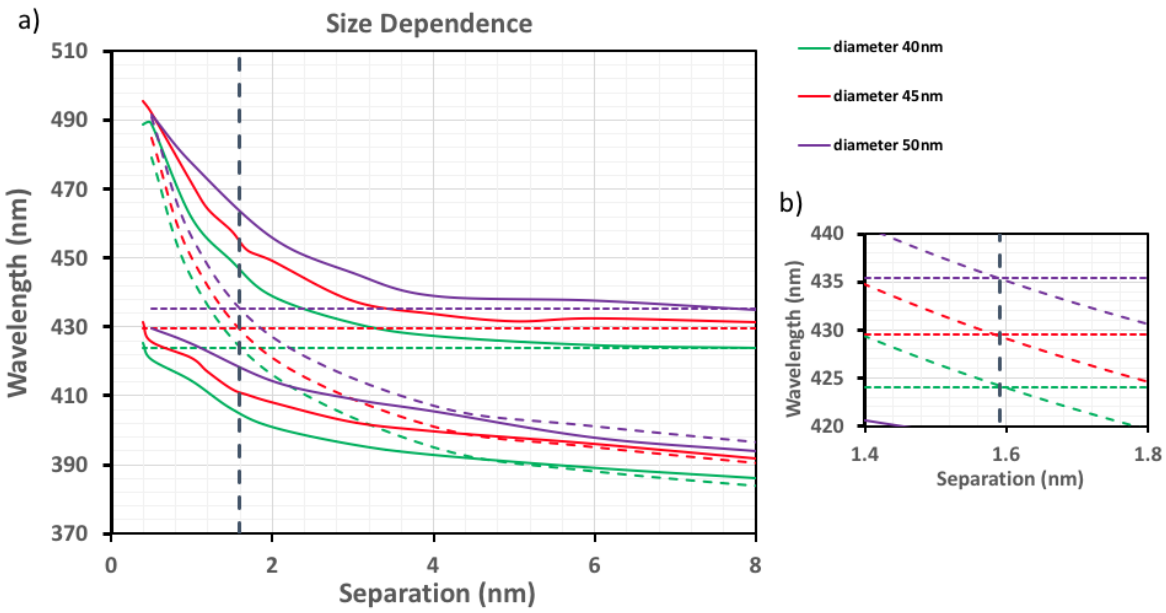

Figure 5.12: a) Simulated size dependence of the plasmonic modes excited in a dipole on a substrate with refractive index n=2.2 by TM polarization. The horizontal lines represent the transverse single sphere modes without coupling and the curved dashed lines represent the longitudinal dipolar modes absent coupling for 40nm sphere (green), 45nm spheres (red), and 50nm spheres (purple). The solid lines represent the modes with coupling. b) Close up of the separation at which the energies of the modes match. Note the separation is independent of the sphere size.

This allows a normalization function to align the avoided level crossing that shifts the spectra linearly based on the size of the spheres in the dipolar pair. This correction is valid within our size distribution of spheres with diameter of 35-50nm but does not extend to much larger spheres that support multiple modes. Most dimers have spheres of slightly different diameters in which case the average sphere size is used to determine the appropriate normalization shift. The separation and size of various dimers was determined from SEM micrographs and the spectral responses measured in PEEM when the exciting light was aligned with the dipole axis. Figure 5.13 shows gaussian fitting determining the resonance peaks of the spectral response for a dipole

with a 6nm separation. The experimentally determined resonances for dipoles of varying separation and size variation of no more than 6nm are then plotted with the calculated modes for a 45nm-45nm dipole on an ITO substrate and the full experimental and simulated spectra are plotted vs sphere separation

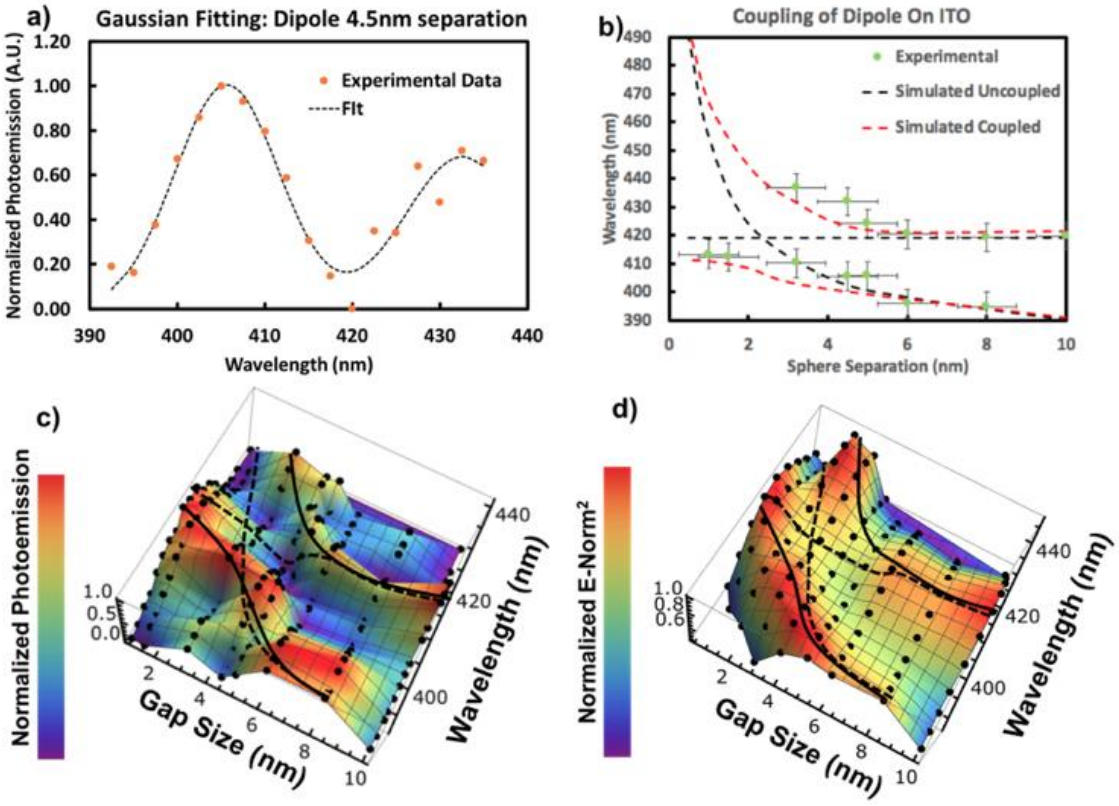

Figure 5.13: a) Fitting of experimental data for a dipole with 4.5nm separation to determine the peaks of the resonances, the peaks correspond to the coupled TSM and LDM. b) Experimentally determined peak resonances for dipoles of varying separation plotted with the simulated response. c) The full experimental data set from eight dimers used in figure 2.17b arranged from largest gap size to smallest gap size. The spectra have been shifted to normalize to a 45nm-45nm dimer. The black dots represent the individual data points in the spectra. Black dashed lines mark the theoretical uncoupled response and solid black guidelines trace out the experimental peaks. d) A 45nm-45nm dipole pair on ITO simulated in COMSOL Multiphysics, the spectra are plotted using the sum of the fitted modes of the LDM and TSM modes.

Figure 5.13 shows good agreement between the experimental and calculated modes showing a distinct avoided level-crossing due to the coupling of the LDM and TSM. This demonstrates PEEM as a tool capable of measuring strong coupling of LSPs through direct imaging of the nearfield plasmonic response. We next consider the impact of the properties of the dielectric substrate on the dimer interaction and consider the case of replacing the dielectric with a conducting substrate.

5.6 Substrate Dependence

The properties of the dielectric substrate play a critical role in how the modes in individual spheres and dimers behave. The resonant wavelength of a single silver particle has been found to be approximately linear with refractive index, the slope of the linear relationship is dependent on the size and material of the particle [86]. For a single metallic nanoparticle on a substrate an analytical method for calculating the plasmonic response is to treat it as being surrounded by a uniform media of a refractive index

$$n_{eff} = \alpha\, n_{media} + (\alpha - 1) n_{substrate}, \tag{5.16}$$

where α is a weighting factor. Then Mie theory can be used to find the expected plasmonic resonance of the particle treating it as a particle in a homogenous media of refractive index n_{eff}. The value of the weighting factor is a matter of some uncertainty with empirical and calculated values ranging from 0.58 to 0.82 [84], and may depend on the size and shape of the particle in question. Using a weighting factor of 0.67 and a Mie theory calculation program available from NanoComposix [107], [108] we find a linear

relationship between the wavelength of the TSM plasmonic mode and the substrate refractive index with good agreement between Mie theory and COMSOL simulations as in Figure 5.14.

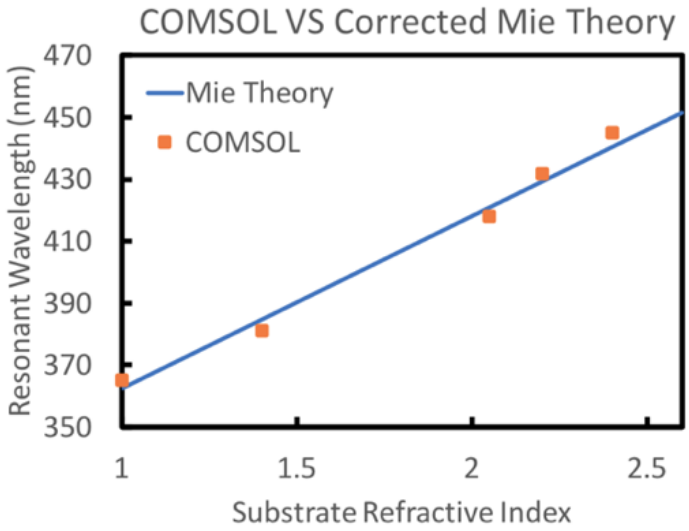

Figure 5.14: Comparison of corrected Mie theory using a weighting factor of 0.67 to calculate an effective index for the media and COMSOL calculations of the transverse single sphere mode of a 45nm diameter silver sphere on substrates of varying refractive indexes.

The index will play a critical role in the avoided level crossing as well. A higher refractive index while red-shifting the TSM, has little effect on the LDM. As a result, the separation of the dimer, at which the mode energies match, occurs at a smaller sphere separation. The efficiency of the coupling increases with closer spacing of the spheres which in turn increases the interaction energy and the magnitude of the splitting of the resonance peaks as predicted by the mathematical model for strong coupling presented in section 4.2. Thus, the magnitude of the avoided level crossing and interaction energy increases with substrate index. This trend is demonstrated in Figure 5.15 by simulated results for silver dimers on substrates with several refractive indexes.

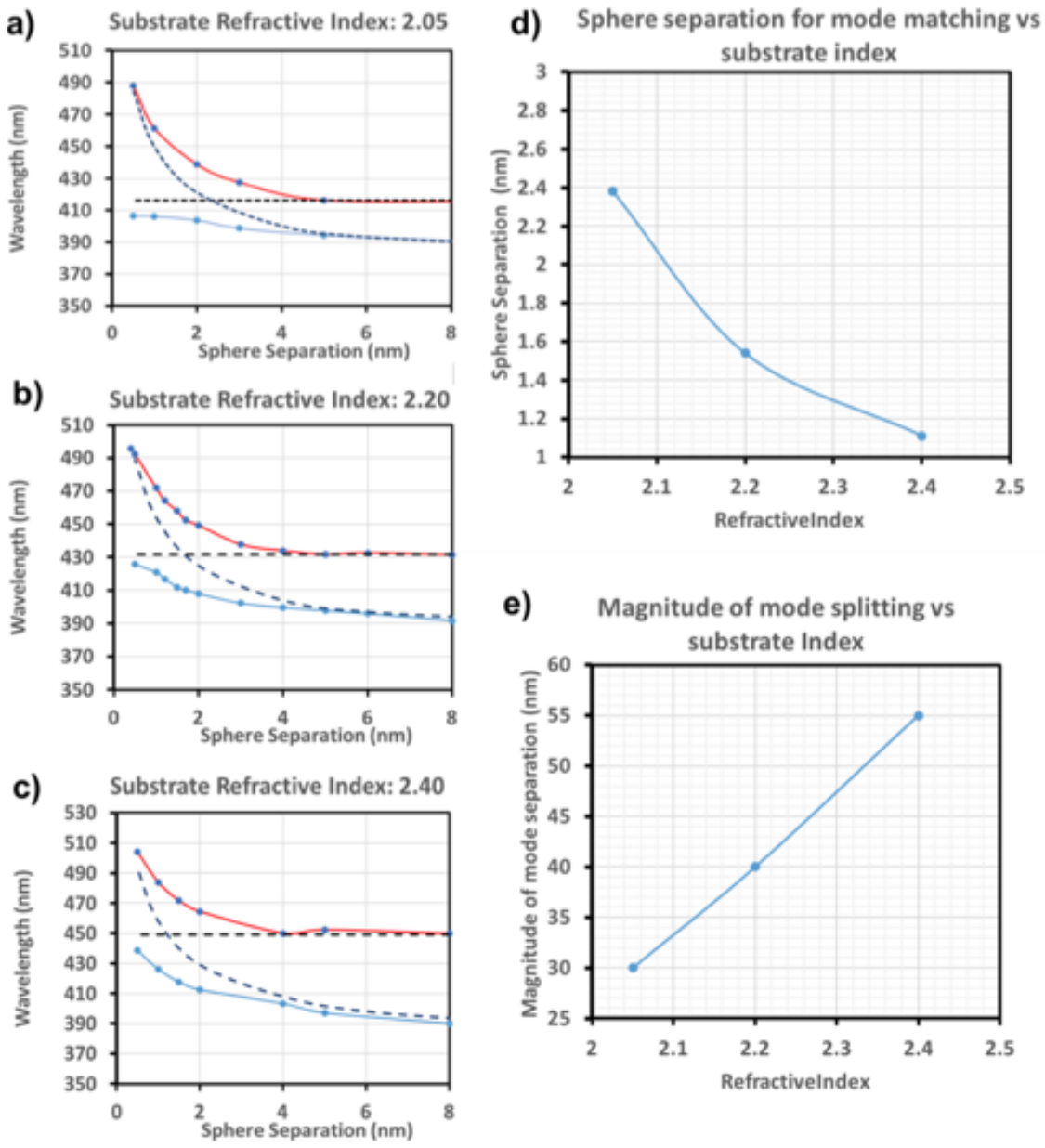

Figure 5.15: a) Simulated dipole coupling for substrates of varying refractive index. The avoided level crossing behavior depends on the refractive index of the substrate. From a-c as the index increases the longitudinal mode increases in wavelength. This causes the avoided level crossing to occur at closer spacing between the spheres. From the simulated dipole coupling for substrates of varying refractive index we see that d) the separation of the spheres that produces a mode energy match decreases as the refractive index increases. e) The magnitude of the splitting increases as the refractive index increases.

When a metallic substrate is introduced replacing the dielectric there are now unbound charges in the substrate and a pathway for charge to transfer from one nanoparticle in the dipole to the other. The oscillation of the electrons through the substrate is termed a charge transfer plasmon (CTP) and introduces an additional mode into the spectra [109]. There is markedly little literature exploring metallic substrate effects on dimer NP-NP interaction. Liu et al. theoretically investigate the coupling of two gold spheres with separation distance on a gold substrate [110]. They demonstrate that the coupling of the 400nm gold particles is modified by the interaction through the substrate. The ability of charge to travel through the substrate produces a charge transfer plasmon. We have run simulations with COMSOL as seen in Figure 5.16 to reproduce Liu's theoretical results and show the presence of a CTP that redshifts as the sphere separation decreases. Wang et al. have shown similar results for gold dipoles on gold substrates [109]. Guang-Can et al. have experimentally shown line-narrowing in the photoluminescence of the dipolar mode in gold dimers on gold substrates, but do not extend the spectra to the frequency necessary to see the CTP [111].

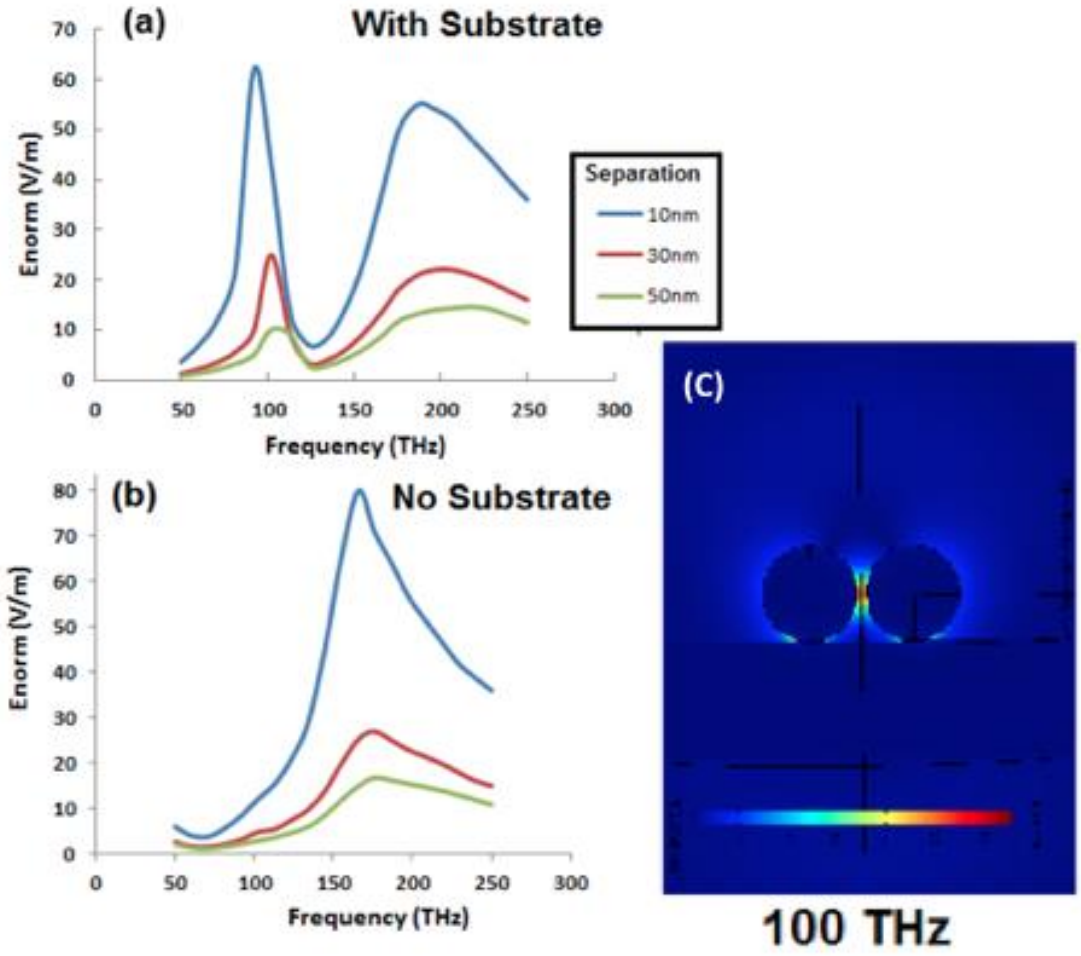

Figure 5.16: Simulation reproducing Liu et al. (a) Electric field with frequency between two 400nm diameter gold spheres on a gold substrate as calculated by COMSOL. The peak at ~100 THz represents the charge transfer plasmon and the peak near 200 THz represents the single sphere mode (b) Electric field with frequency between two 400nm diameter gold spheres with no substrate. (c) Snapshot of the COMSOL simulation for 10nm separation. Scale bar represent the normalized electromagnetic field.

Notably the CTP mediated by the substrate will always be red shifted from the LDM, this can be understood qualitatively by considering the path of the charge oscillations. The LDM is excited when the charge oscillates along the diameter of the dimer, the CTP takes the longer path through the substrate. The greater path length through the substrate requires a lower driving frequency, or a red-shifted wavelength. It is then

impossible to produce a mode energy match between the LDM and CTP for spherical particles as the gap size must reduce to less than zero, merging the two particles.

Silver particles on a gold substrate produce similar effects, both the coupling effects between the TSM and LDM observed on ITO and the charge transfer plasmon are present. The real part of the refractive index of gold in the 390nm-450nm range is in the range of ~1.5-1.4. This is considerably lower than the ~2.1 refractive index of ITO so produces a much smaller red-shift of the TSM. This means that the avoided level-crossing occurs at a greater sphere separation and thus the interaction energy and the magnitude of the avoided level crossing will be less. The simulated plasmonic response of a dimer with 50nm spheres and varying gap size is shown in Figure 5.17b, note the energy match between the LDM and TSM occurs at a separation of ~7nm, at this separation the LDM is very weak and avoided level crossing in minimal.

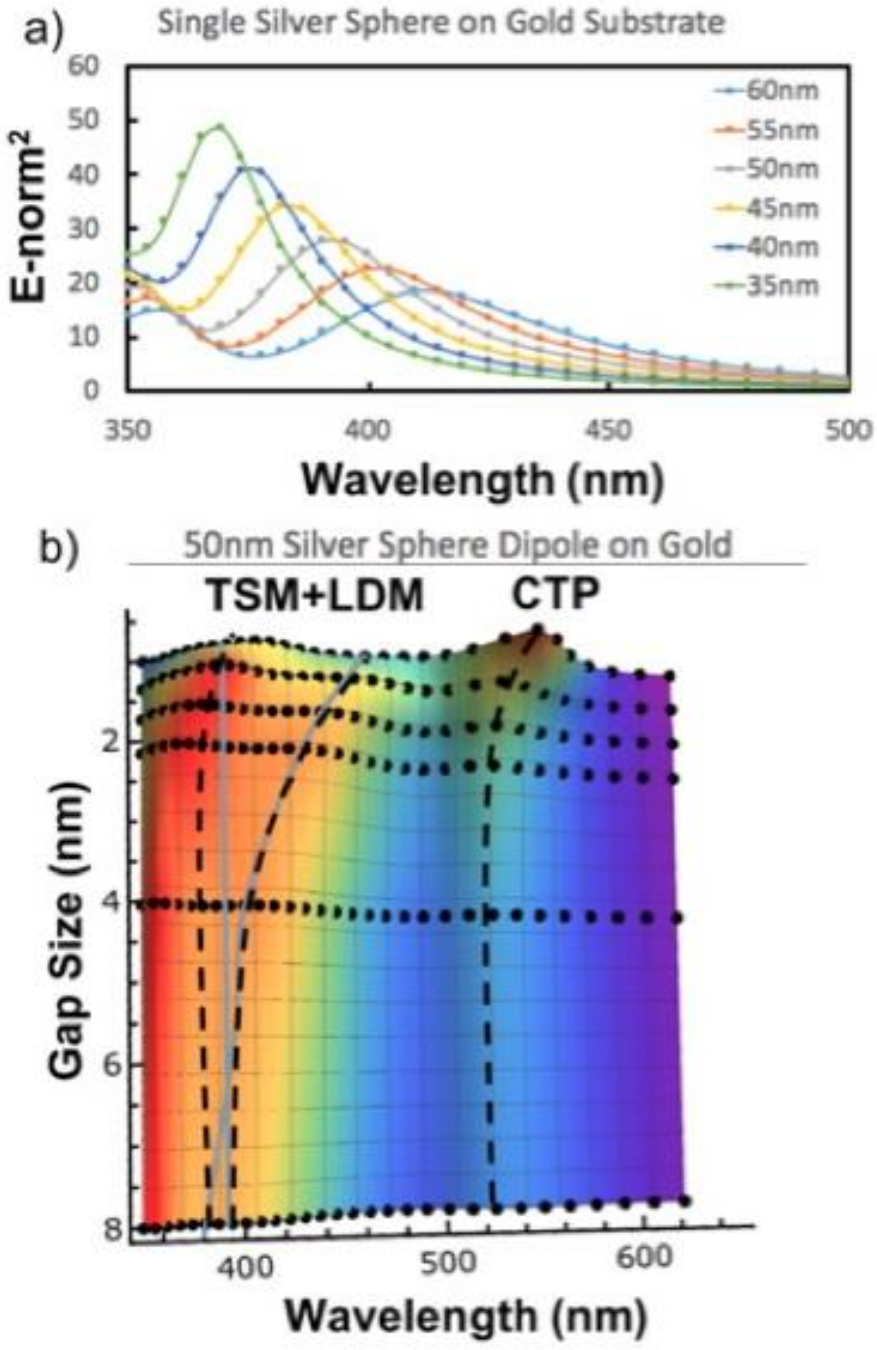

Figure 5.17: a) Simulated response of a silver sphere on a gold substrate for varying sphere size. b) Simulated response of a silver sphere dimer with 50nm diameter spheres on a gold substrate. The transverse single sphere mode, longitudinal dipolar mode, and charge transfer plasmon mode are indicated with dashed black lines and the expected uncoupled behavior is indicated by grey lines.

From Figure 5.17a we see a sphere size of ~60nm would be needed to put the resonance peak of a silver nanosphere on a gold substrate within the frequency range available in our microscope. The larger sphere size, however, also comes with a broader resonance which is not easily resolvable within the accessible frequency range of our laser. Simulations shown in Figure 5.17b demonstrate the plasmonic responses expected for gold substrate and 50nm dimer, these results would theoretical be reproducible using PEEM and the techniques as presented here for silver spheres on ITO provided a light source that is tunable in the appropriate range.

The substrate dependence of plasmonic dimer modes raises some other intriguing possibilities. Higher index conductive materials such as doped silicon could be used to produce a stronger coupling and greater mode splitting while also producing a charge transfer plasmon. The refractive index of doped amorphous silicon depends on the doping level and could be used to tune the refractive index of a substrate and thus the plasmonic dimer modes. With our methodology PEEM is a valuable tool for future exploration of substrate effects on nanoscale plasmonic resonances.

6 Conclusions

We have demonstrated the versatility of PEEM as a tool for observation and characterization of plasmonic and photonic phenomena. We have examined a finite thin-film photonic crystal waveguide with asymmetric vertical geometry. Through direct imaging of the defect channel mode PEEM allows for an experimental determination of the guided photonic modes and resonances. Such a detailed and quantitative optical characterization of these structures is a step forward in the technical development of these structures and may contribute to a more complete understanding of the spatial mode distributions and power flow in integrated photonic devices. In future work a spatial evaluation of optical wave fronts and even an imaging of their time evolution appears possible in PEEM. Pump-probe methodology towards this goal is a current area of research in our group.

We have also detailed the plasmonic response of monomer and dimer arrangements of nanoparticles on a substrate at oblique incidence, i.e. under low-symmetry conditions. These systems feature a complicated system of interacting eigenmodes and hold considerable importance for development of future nanoscale devices from sensors to integrated circuits. PEEM's high resolution and noninvasive imaging is a powerful tool for a fundamental characterization. Measuring the plasmonic responses we have demonstrated the ability to determine and identify spectral characteristics, polarization dependencies as well as non-linear phenomena such as optical strong coupling and

avoided level-crossing. An improved understanding of the optical behavior of these fundamental systems is needed to develop new devices for optical and plasmonic control, optical switching and processing, field confinement, plasmon-enhanced lasing and the exploration of other new optical devices with nanometer dimensions.

Bibliography

[1] A. Yang *et al.*, "Real-time tunable lasing from plasmonic nanocavity arrays," *Nat. Commun.*, vol. 6, Apr. 2015, doi: 10.1038/ncomms7939.

[2] C. Zhang *et al.*, "Plasmonic lasing of nanocavity embedding in metallic nanoantenna array," *Nano Lett.*, vol. 15, no. 2, pp. 1382–1387, Feb. 2015, doi: 10.1021/nl504689s.

[3] H. A. Atwater and A. Polman, "Plasmonics for improved photovoltaic devices," *Nature Materials*, vol. 9, no. 3. Nat Mater, pp. 205–213, Mar-2010, doi: 10.1038/nmat2629.

[4] S. Pillai and M. A. Green, "Plasmonics for photovoltaic applications," in *Solar Energy Materials and Solar Cells*, 2010, vol. 94, no. 9, pp. 1481–1486, doi: 10.1016/j.solmat.2010.02.046.

[5] J. A. Gordon and R. W. Ziolkowski, "The design and simulated performance of a coated nano-particle laser," *Opt. Express*, vol. 15, no. 5, p. 2622, Mar. 2007, doi: 10.1364/oe.15.002622.

[6] K. C. Y. Huang, M. K. Seo, T. Sarmiento, Y. Huo, J. S. Harris, and M. L. Brongersma, "Electrically driven subwavelength optical nanocircuits," *Nat. Photonics*, vol. 8, no. 3, pp. 244–249, Mar. 2014, doi: 10.1038/nphoton.2014.2.

[7] M. S. Tame, K. R. McEnery, S. K. Ozdemir, J. Lee, S. A. Maier, and M. S. Kim, "Quantum Plasmonics," *Nat. Phys.*, vol. 9, no. 6, pp. 329–340, Dec. 2013, doi: 10.1038/nphys2615.

[8] J. S. Fakonas, H. Lee, Y. A. Kelaita, and H. A. Atwater, "Two-plasmon quantum interference," *Nat. Photonics*, vol. 8, no. 4, pp. 317–320, Mar. 2014, doi: 10.1038/nphoton.2014.40.

[9] Y. He, R. Rappuoli, A. S. De Groot, and R. T. Chen, "Emerging vaccine informatics," *Journal of Biomedicine and Biotechnology*, vol. 2010. J Biomed Biotechnol, 2010, doi: 10.1155/2010/218590.

[10] D. E. Chang, A. S. Sørensen, E. A. Demler, and M. D. Lukin, "A single-photon transistor using nanoscale surface plasmons," *Nat. Phys.*, vol. 3, no. 11, pp. 807–812, Aug. 2007, doi: 10.1038/nphys708.

[11] S. Medhekar and R. K. Sarkar, "All-optical passive transistor," *Opt. Lett.*, vol. 30, no. 8, p. 887, Apr. 2005, doi: 10.1364/ol.30.000887.

[12] J. A. Schuller, E. S. Barnard, W. Cai, Y. C. Jun, J. S. White, and M. L. Brongersma, "Plasmonics for extreme light concentration and manipulation," *Nature Materials*, vol. 9, no. 3. Nature Publishing Group, pp. 193–204, 19-Feb-2010, doi: 10.1038/nmat2630.

[13] T. J. Davis, D. E. Gómez, and A. Roberts, "Plasmonic circuits for manipulating optical information," *Nanophotonics*, vol. 6, no. 3. Walter de Gruyter GmbH, pp. 543–559, 01-May-2017, doi: 10.1515/nanoph-2016-0131.

[14] E. Brüche, "Elektronenmikroskopische Abbildung mit lichtelektrischen Elektronen," *Zeitschrift für Phys.*, vol. 86, no. 7–8, pp. 448–450, Jul. 1933, doi: 10.1007/BF01341360.

[15] E. Bauer, “Low energy electron microscopy,” *Reports on Progress in Physics*, vol. 57, no. 9. IOP Publishing, pp. 895–938, 01-Sep-1994, doi: 10.1088/0034-4885/57/9/002.
[16] E. Bauer, “Leem basics,” *Surf. Rev. Lett.*, vol. 5, no. 6, pp. 1275–1286, Jan. 1998, doi: 10.1142/S0218625X98001614.
[17] G. F. Rempfer, W. P. Skoczylas, and O. H. Griffith, “Design and performance of a high-resolution photoelectron microscope.,” *Ultramicroscopy*, vol. 36, no. 1–3, pp. 196–221, May 1991, doi: 10.1016/0304-3991(91)90151-u.
[18] G. F. Rempfer, D. M. Desloge, W. P. Skoczylas, and O. H. Griffith, “Simultaneous correction of spherical and chromatic aberrations with an electron mirror: An electron optical achromat,” *Microsc. Microanal.*, vol. 3, no. 1, pp. 14–27, 1997, doi: 10.1017/S143192769797001X.
[19] G. F. Rempfer, “Unipotential electrostatic lenses: Paraxial properties and aberrations of focal length and focal point,” *J. Appl. Phys.*, vol. 57, no. 7, pp. 2385–2401, 1985, doi: 10.1063/1.334347.
[20] “Relationship of lens aberrations to image aberrations in electron optics.” [Online]. Available: https://www.researchgate.net/publication/287749493_Relationship_of_lens_aberrations_to_image_aberrations_in_electron_optics. [Accessed: 21-Jan-2020].
[21] R. Könenkamp *et al.*, “Image properties in an aberration-corrected photoemission electron microscope,” in *Physics Procedia*, 2008, vol. 1, no. 1, pp. 505–511, doi: 10.1016/j.phpro.2008.07.132.
[22] R. Könenkamp, R. C. Word, G. F. Rempfer, T. Dixon, L. Almaraz, and T. Jones, “5.4nm spatial resolution in biological photoemission electron microscopy,” *Ultramicroscopy*, vol. 110, no. 7, pp. 899–902, Jun. 2010, doi: 10.1016/j.ultramic.2010.04.005.
[23] J. Fitzgerald, “Aberration Corrected Photoemission Electron Microscopy with Photonics Applications,” Portland, OR, Jan. 2000.
[24] M. Merschdorf, W. Pfeiffer, A. Thon, S. Voll, and G. Gerber, “Photoemission from multiply excited surface plasmons in Ag nanoparticles,” *Appl. Phys. A Mater. Sci. Process.*, vol. 71, no. 5, pp. 547–552, Nov. 2000, doi: 10.1007/s003390000712.
[25] D. L. Habliston, G. B. Birrell, O. H. Griffith, and G. F. Rempfer, “Photoelectron imaging of DNA: a study of substrates and contrast,” *J. Phys. Chem.*, vol. 97, no. 12, pp. 3022–3027, Mar. 1993, doi: 10.1021/j100114a032.
[26] O. H. Griffith, D. L. Habliston, G. B. Birrell, W. P. Skoczylas, and K. K. Hedberg, “Biological photocathodes.,” *Proc. Natl. Acad. Sci. U. S. A.*, vol. 86, no. 6, pp. 1826–1830, 1989, doi: 10.1073/pnas.86.6.1826.
[27] O. H. Griffith and G. F. Rempfer, “Photoelectron imaging and photoelectron labeling,” *Ultramicroscopy*, vol. 24, no. 2–3, pp. 299–312, 1988, doi: 10.1016/0304-3991(88)90317-8.
[28] A. D. Smith, G. Cressey, P. F. Schofield, and B. A. Cressey, “Development of X-ray photoemission electron microscopy (X-PEEM) at the SRS,” *J. Synchrotron Radiat.*, vol. 5, no. 3, pp. 1108–1110, May 1998, doi: 10.1107/S0909049597015811.

[29] L. Le Guyader *et al.*, “Studying nanomagnets and magnetic heterostructures with X-ray PEEM at the Swiss Light Source,” *J. Electron Spectros. Relat. Phenomena*, vol. 185, no. 10, pp. 371–380, 2012, doi: 10.1016/j.elspec.2012.03.001.
[30] S. Anders *et al.*, “Photoemission electron microscope for the study of magnetic materials,” *Rev. Sci. Instrum.*, vol. 70, no. 10, pp. 3973–3981, 1999, doi: 10.1063/1.1150023.
[31] J. Vogel *et al.*, “Time-resolved magnetic domain imaging by x-ray photoemission electron microscopy,” *Appl. Phys. Lett.*, vol. 82, no. 14, pp. 2299–2301, Apr. 2003, doi: 10.1063/1.1564876.
[32] A. Kubo, K. Onda, H. Petek, Z. Sun, Y. S. Jung, and H. K. Kim, “Femtosecond imaging of surface plasmon dynamics in a nanostructured silver film,” *Nano Lett.*, vol. 5, no. 6, pp. 1123–1127, Jun. 2005, doi: 10.1021/nl0506655.
[33] Y. Gong, A. G. Joly, D. Hu, P. Z. El-Khoury, and W. P. Hess, “Ultrafast Imaging of Surface Plasmons Propagating on a Gold Surface,” *Nano Lett.*, vol. 15, no. 5, pp. 3472–3478, May 2015, doi: 10.1021/acs.nanolett.5b00803.
[34] G. Razinskas *et al.*, “Normal-Incidence PEEM Imaging of Propagating Modes in a Plasmonic Nanocircuit,” *Nano Lett.*, vol. 16, no. 11, pp. 6832–6837, Nov. 2016, doi: 10.1021/acs.nanolett.6b02569.
[35] C. Lemke *et al.*, “Spatiotemporal Characterization of SPP Pulse Propagation in Two-Dimensional Plasmonic Focusing Devices,” *Nano Lett.*, vol. 13, no. 3, pp. 1053–1058, Mar. 2013, doi: 10.1021/nl3042849.
[36] C. Lemke *et al.*, “Mapping surface plasmon polariton propagation via counter-propagating light pulses,” *Opt. Express*, vol. 20, no. 12, p. 12877, Jun. 2012, doi: 10.1364/oe.20.012877.
[37] R. C. Word and R. Könenkamp, “Photonic and plasmonic surface field distributions characterized with normal- and oblique-incidence multi-photon PEEM,” *Ultramicroscopy*, vol. 183, pp. 1339–1351, Dec. 2017, doi: 10.1016/j.ultramic.2017.05.012.
[38] R. C. Word and R. Könenkamp, “Mode structure of planar optical antennas on dielectric substrates,” *Opt. Express*, vol. 24, no. 16, p. 18727, Aug. 2016, doi: 10.1364/oe.24.018727.
[39] R. C. Word, J. P. S. Fitzgerald, and R. Könenkamp, “Positional control of plasmonic fields and electron emission,” *Appl. Phys. Lett.*, vol. 105, no. 11, Sep. 2014, doi: 10.1063/1.4896111.
[40] R. Könenkamp, R. C. Word, J. Fitzgerald, A. Nadarajah, and S. Saliba, “Controlled spatial switching and routing of surface plasmons in designed single-crystalline gold nanostructures,” *Appl. Phys. Lett.*, vol. 101, no. 14, Oct. 2012, doi: 10.1063/1.4757125.
[41] R. C. Word, J. P. S. Fitzgerald, and R. Könenkamp, “Direct imaging of optical diffraction in photoemission electron microscopy,” *Appl. Phys. Lett.*, vol. 103, no. 2, Jul. 2013, doi: 10.1063/1.4813550.
[42] J. P. S. Fitzgerald, R. C. Word, and R. Könenkamp, “Subwavelength visualization of light in thin film waveguides with photoelectrons,” *Phys. Rev. B - Condens. Matter*

Mater. Phys., vol. 89, no. 19, May 2014, doi: 10.1103/PhysRevB.89.195129.
[43] J. P. S. Fitzgerald, R. C. Word, S. D. Saliba, and R. Könenkamp, "Photonic near-field imaging in multiphoton photoemission electron microscopy," *Phys. Rev. B - Condens. Matter Mater. Phys.*, vol. 87, no. 20, May 2013, doi: 10.1103/PhysRevB.87.205419.
[44] R. C. Word, J. P. S. Fitzgerald, and R. Könenkamp, "Direct coupling of photonic modes and surface plasmon polaritons observed in 2-photon PEEM," *Opt. Express*, vol. 21, no. 25, p. 30507, Dec. 2013, doi: 10.1364/oe.21.030507.
[45] T. Stenmark, R. C. Word, and R. Könenkamp, "Confined photonic mode propagation observed in photoemission electron microscopy," *Ultramicroscopy*, vol. 183, 2017, doi: 10.1016/j.ultramic.2017.06.013.
[46] T. Stenmark, R. C. Word, and R. Könenkamp, "Determination of the Goos-Hänchen shift in dielectric waveguides via photo emission electron microscopy in the visible spectrum," *Opt. Express*, vol. 24, no. 4, 2016, doi: 10.1364/OE.24.003839.
[47] T. Stenmark and R. Könenkamp, "Photoemission electron microscopy to characterize slow light in a photonic crystal line defect," *Phys. Rev. B*, vol. 99, no. 20, 2019, doi: 10.1103/PhysRevB.99.205428.
[48] R. C. Word, J. P. S. Fitzgerald, and R. Könenkamp, "Light propagation and interaction observed with electrons," *Ultramicroscopy*, vol. 160, pp. 84–89, Jan. 2016, doi: 10.1016/j.ultramic.2015.10.005.
[49] F. Schertz, M. Schmelzeisen, M. Kreiter, H. J. Elmers, and G. Schönhense, "Field emission of electrons generated by the near field of strongly coupled plasmons," *Phys. Rev. Lett.*, vol. 108, no. 23, p. 237602, Jun. 2012, doi: 10.1103/PhysRevLett.108.237602.
[50] F. Schertz, M. Schmelzeisen, R. Mohammadi, M. Kreiter, H. J. Elmers, and G. Schönhense, "Near field of strongly coupled plasmons: Uncovering dark modes," *Nano Lett.*, vol. 12, no. 4, pp. 1885–1890, Apr. 2012, doi: 10.1021/nl204277y.
[51] M. V. Fedorov, "L. V. Keldysh's 'Ionization in the Field of a Strong Electromagnetic Wave' and modern physics of atomic interaction with a strong laser field," *J. Exp. Theor. Phys.*, vol. 122, no. 3, pp. 449–455, 2016, doi: 10.1134/S1063776116030043.
[52] P. A. Bobbert and J. Vlieger, "Light scattering by a sphere on a substrate," *Phys. A Stat. Mech. its Appl.*, vol. 137, no. 1–2, pp. 209–242, Jul. 1986, doi: 10.1016/0378-4371(86)90072-5.
[53] N. Hooshmand and M. A. El-Sayed, "Collective multipole oscillations direct the plasmonic coupling at the nanojunction interfaces," *Proc. Natl. Acad. Sci. U. S. A.*, vol. 116, no. 39, pp. 19299–19304, Sep. 2019, doi: 10.1073/pnas.1909416116.
[54] S. K. Ghosh and T. Pal, "Interparticle coupling effect on the surface plasmon resonance of gold nanoparticles: From theory to applications," *Chemical Reviews*, vol. 107, no. 11. American Chemical Society , pp. 4797–4862, Nov-2007, doi: 10.1021/cr0680282.
[55] X. Fan, W. Zheng, and D. J. Singh, "Light scattering and surface plasmons on small

spherical particles," *Light: Science and Applications*, vol. 3, no. 6. Nature Publishing Group, pp. e179–e179, 06-Jun-2014, doi: 10.1038/lsa.2014.60.
[56] V. L. Y. Loke *et al.*, "Comparison between discrete dipole approximation and other modelling methods for the plasmonic response of gold nanospheres," *Appl. Phys. B Lasers Opt.*, vol. 115, no. 2, pp. 237–246, Aug. 2014, doi: 10.1007/s00340-013-5594-z.
[57] M. A. Yurkin and M. Huntemann, "Rigorous and Fast Discrete Dipole Approximation for Particles near a Plane Interface," *J. Phys. Chem. C*, vol. 119, no. 52, pp. 29088–29094, Dec. 2015, doi: 10.1021/acs.jpcc.5b09271.
[58] J. A. Waxenegger, "Simulation of plasmonic nanoparticles situated on substrates," University of Graz, 2016.
[59] E. R. Encina and E. A. Coronado, "Plasmon coupling in silver nanosphere pairs," *J. Phys. Chem. C*, vol. 114, no. 9, pp. 3918–3923, Mar. 2010, doi: 10.1021/jp912096v.
[60] C. G. Khoury, S. J. Norton, and T. Vodinh, "Plasmonics of 3-D nanoshell dimers using multipole expansion and finite element method," *ACS Nano*, vol. 3, no. 9, pp. 2776–2788, Sep. 2009, doi: 10.1021/nn900664j.
[61] H. Cha, D. Lee, J. H. Yoon, and S. Yoon, "Plasmon coupling between silver nanoparticles: Transition from the classical to the quantum regime," *J. Colloid Interface Sci.*, vol. 464, pp. 18–24, Feb. 2016, doi: 10.1016/j.jcis.2015.11.009.
[62] P. B. Johnson and R. W. Christy, "Optical constants of the noble metals," *Phys. Rev. B*, vol. 6, no. 12, pp. 4370–4379, Dec. 1972, doi: 10.1103/PhysRevB.6.4370.
[63] *Guided-Wave Optoelectronics*. Springer US, 1995.
[64] E. Dulkeith, F. Xia, L. Schares, W. M. J. Green, and Y. A. Vlasov, "Group index and group velocity dispersion in silicon-on-insulator photonic wires," *Opt. Express*, vol. 14, no. 9, p. 3853, 2006, doi: 10.1364/oe.14.003853.
[65] S. M. Israelsen, M. A. U. Castaneda, and K. Rottwitt, "Determining the group velocity dispersion by field analysis for the LP0X, LP1X, and LP2X mode groups independently of the fiber length: Applications to step-index fibers," *J. Opt. Soc. Am. B Opt. Phys.*, vol. 34, no. 1, pp. 7–11, 2017, doi: 10.1364/JOSAB.34.000007.
[66] H. Wen, M. Terrel, S. Fan, and M. Digonnet, "Sensing with slow light in fiber Bragg gratings," *IEEE Sens. J.*, vol. 12, no. 1, pp. 156–163, 2012, doi: 10.1109/JSEN.2011.2135343.
[67] S. Takahashi *et al.*, "Direct creation of three-dimensional photonic crystals by a top-down approach," *Nat. Mater.*, vol. 8, no. 9, pp. 721–725, 2009, doi: 10.1038/nmat2507.
[68] D. George *et al.*, "Holographic fabrication of 3D photonic crystals through interference of multi-beams with 4 + 1, 5 + 1 and 6 + 1 configurations," *Opt. Express*, vol. 22, no. 19, p. 22421, Sep. 2014, doi: 10.1364/oe.22.022421.
[69] H. Zhang, H. Zhu, L. Qian, and D. Fan, "Analysis of leaky modes of photonic crystal slabs with deeply patterned lattice," *J. Opt. A Pure Appl. Opt.*, vol. 8, no. 5, pp. 483–488, May 2006, doi: 10.1088/1464-4258/8/5/019.
[70] "Photonic Crystals: Molding the Flow of Light." [Online]. Available: http://ab-

initio.mit.edu/book/. [Accessed: 21-Jan-2020].
[71] A. Y. Petrov and M. Eich, “Zero dispersion at small group velocities in photonic crystal waveguides,” *Appl. Phys. Lett.*, vol. 85, no. 21, pp. 4866–4868, Nov. 2004, doi: 10.1063/1.1815066.
[72] S. G. Johnson, P. R. Villeneuve, S. Fan, and J. D. Joannopoulos, “Linear waveguides in photonic-crystal slabs,” *Phys. Rev. B - Condens. Matter Mater. Phys.*, vol. 62, no. 12, pp. 8212–8222, Sep. 2000, doi: 10.1103/PhysRevB.62.8212.
[73] D. K. Gramotnev and S. I. Bozhevolnyi, “Plasmonics beyond the diffraction limit,” *Nature Photonics*, vol. 4, no. 2. Nature Publishing Group, pp. 83–91, Feb-2010, doi: 10.1038/nphoton.2009.282.
[74] A. J. Haes and R. P. Van Duyne, “A nanoscale optical biosensor: Sensitivity and selectivity of an approach based on the localized surface plasmon resonance spectroscopy of triangular silver nanoparticles,” *J. Am. Chem. Soc.*, vol. 124, no. 35, pp. 10596–10604, Sep. 2002, doi: 10.1021/ja020393x.
[75] N. Nath and A. Chilkoti, “Label-free biosensing by surface plasmon resonance of nanoparticles on glass: Optimization of nanoparticle size,” *Anal. Chem.*, vol. 76, no. 18, pp. 5370–5378, Sep. 2004, doi: 10.1021/ac049741z.
[76] P. Alivisatos, “The use of nanocrystals in biological detection,” *Nature Biotechnology*, vol. 22, no. 1. pp. 47–52, Jan-2004, doi: 10.1038/nbt927.
[77] S. S. Shankar, A. Rai, A. Ahmad, and M. Sastry, “Rapid synthesis of Au, Ag, and bimetallic Au core-Ag shell nanoparticles using Neem (Azadirachta indica) leaf broth,” *J. Colloid Interface Sci.*, vol. 275, no. 2, pp. 496–502, Jul. 2004, doi: 10.1016/j.jcis.2004.03.003.
[78] K. N. Thakkar, S. S. Mhatre, and R. Y. Parikh, “Biological synthesis of metallic nanoparticles,” *Nanomedicine: Nanotechnology, Biology, and Medicine*, vol. 6, no. 2. pp. 257–262, Apr-2010, doi: 10.1016/j.nano.2009.07.002.
[79] V. Amendola, O. M. Bakr, and F. Stellacci, “A study of the surface plasmon resonance of silver nanoparticles by the discrete dipole approximation method: Effect of shape, size, structure, and assembly,” *Plasmonics*, vol. 5, no. 1, pp. 85–97, Mar. 2010, doi: 10.1007/s11468-009-9120-4.
[80] Y. Xia and N. J. Halas, “Shape-Controlled Synthesis and Surface Plasmonic Properties of Metallic Nanostructures,” *MRS Bull.*, vol. 30, no. 5, pp. 338–348, May 2005, doi: 10.1557/mrs2005.96.
[81] C. Noguez, “Surface plasmons on metal nanoparticles: The influence of shape and physical environment,” *J. Phys. Chem. C*, vol. 111, no. 10, pp. 3606–3619, Mar. 2007, doi: 10.1021/jp066539m.
[82] J. J. Mock, D. R. Smith, and S. Schultz, “Local refractive index dependence of plasmon resonance spectra from individual nanoparticles,” *Nano Lett.*, vol. 3, no. 4, pp. 485–491, Apr. 2003, doi: 10.1021/nl0340475.
[83] A. Pinchuk, A. Hilger, G. Von Plessen, and U. Kreibig, “Substrate effect on the optical response of silver nanoparticles,” *Nanotechnology*, vol. 15, no. 12, pp. 1890–1896, Dec. 2004, doi: 10.1088/0957-4484/15/12/036.
[84] A. Curry, G. Nusz, A. Chilkoti, and A. Wax, “Substrate effect on refractive index

dependence of plasmon resonance for individual silver nanoparticles observed using darkfield microspectroscopy," *Opt. Express*, vol. 13, no. 7, p. 2668, Apr. 2005, doi: 10.1364/opex.13.002668.

[85] M. M. Miller and A. A. Lazarides, "Sensitivity of metal nanoparticle surface plasmon resonance to the dielectric environment," *J. Phys. Chem. B*, vol. 109, no. 46, pp. 21556–21565, Nov. 2005, doi: 10.1021/jp054227y.

[86] M. D. Malinsky, K. Lance Kelly, G. C. Schatz, and R. P. van Duyne, "Nanosphere lithography: effect of substrate on the localized surface plasmon resonance spectrum of silver nanoparticles," *J. Phys. Chem. B*, vol. 105, no. 12, pp. 2343–2350, Mar. 2001, doi: 10.1021/jp002906x.

[87] Y. Uchiho and K. Kajikawa, "Evaluation of gap distance between gold nanospheres and a gold substrate by absorption spectroscopy," *Chem. Phys. Lett.*, vol. 478, no. 4–6, pp. 211–214, Aug. 2009, doi: 10.1016/j.cplett.2009.07.076.

[88] T. Okamoto and I. Yamaguchi, "Optical Absorption Study of the Surface Plasmon Resonance in Gold Nanoparticles Immobilized onto a Gold Substrate by Self-Assembly Technique," *J. Phys. Chem. B*, vol. 107, no. 38, pp. 10321–10324, Sep. 2003, doi: 10.1021/jp034537l.

[89] G. Xu, Y. Chen, M. Tazawa, and P. Jin, "Influence of dielectric properties of a substrate upon plasmon resonance spectrum of supported Ag nanoparticles," *Appl. Phys. Lett.*, vol. 88, no. 4, pp. 1–3, 2006, doi: 10.1063/1.2167827.

[90] J. J. Mock, R. T. Hill, A. Degiron, S. Zauscher, A. Chilkoti, and D. R. Smith, "Distance-dependent plasmon resonant coupling between a gold nanoparticle and gold film," *Nano Lett.*, vol. 8, no. 8, pp. 2245–2252, Aug. 2008, doi: 10.1021/nl080872f.

[91] T. Atay, J. H. Song, and A. V. Nurmikko, "Strongly interacting plasmon nanoparticle pairs: From dipole-dipole interaction to conductively coupled regime," *Nano Lett.*, vol. 4, no. 9, pp. 1627–1631, Sep. 2004, doi: 10.1021/nl049215n.

[92] A. M. Funston, C. Novo, T. J. Davis, and P. Mulvaney, "Plasmon coupling of gold nanorods at short distances and in different geometries," *Nano Lett.*, vol. 9, no. 4, pp. 1651–1658, Apr. 2009, doi: 10.1021/nl900034v.

[93] M. Danckwerts and L. Novotny, "Optical frequency mixing at coupled gold nanoparticles," *Phys. Rev. Lett.*, vol. 98, no. 2, p. 026104, Jan. 2007, doi: 10.1103/PhysRevLett.98.026104.

[94] H. Tamaru, H. Kuwata, H. T. Miyazaki, and K. Miyano, "Resonant light scattering from individual Ag nanoparticles and particle pairs," *Appl. Phys. Lett.*, vol. 80, no. 10, pp. 1826–1828, Mar. 2002, doi: 10.1063/1.1461072.

[95] L. Gunnarsson *et al.*, "Confined plasmons in nanofabricated single silver particle pairs: Experimental observations of strong interparticle interactions," *J. Phys. Chem. B*, vol. 109, no. 3, pp. 1079–1087, Jan. 2005, doi: 10.1021/jp049084e.

[96] I. Romero, J. Aizpurua, G. W. Bryant, and F. J. García De Abajo, "Plasmons in nearly touching metallic nanoparticles: singular response in the limit of touching dimers," *Opt. Express*, vol. 14, no. 21, p. 9988, Oct. 2006, doi:

10.1364/oe.14.009988.
[97] S. Sheikholeslami, Y. W. Jun, P. K. Jain, and A. P. Alivisatos, “Coupling of optical resonances in a compositionally asymmetric plasmonic nanoparticle dimer,” *Nano Lett.*, vol. 10, no. 7, pp. 2655–2660, Jul. 2010, doi: 10.1021/nl101380f.
[98] S. C. Yang *et al.*, “Plasmon hybridization in individual gold nanocrystal dimers: Direct observation of bright and dark modes,” *Nano Lett.*, vol. 10, no. 2, pp. 632–637, Feb. 2010, doi: 10.1021/nl903693v.
[99] L. Novotny, “Strong coupling, energy splitting, and level crossings: A classical perspective,” *Am. J. Phys.*, vol. 78, no. 11, pp. 1199–1202, Nov. 2010, doi: 10.1119/1.3471177.
[100] A. R. B. De Magalhães, C. H. D’Ávila Fonseca, and M. C. Nemes, “Classical and quantum coupled oscillators: Symplectic structure,” *Phys. Scr.*, vol. 74, no. 4, pp. 472–480, Oct. 2006, doi: 10.1088/0031-8949/74/4/011.
[101] L. Schumacher *et al.*, “Precision Plasmonics with Monomers and Dimers of Spherical Gold Nanoparticles: Nonequilibrium Dynamics at the Time and Space Limits,” *J. Phys. Chem. C*, vol. 123, no. 21, pp. 13181–13191, May 2019, doi: 10.1021/acs.jpcc.9b01007.
[102] H. Yu *et al.*, “Exploring Coupled Plasmonic Nanostructures in the Near Field by Photoemission Electron Microscopy,” *ACS Nano*, vol. 10, no. 11, pp. 10373–10381, Nov. 2016, doi: 10.1021/acsnano.6b06206.
[103] J. Yang *et al.*, “Manipulation of the dephasing time by strong coupling between localized and propagating surface plasmon modes,” *Nat. Commun.*, vol. 9, no. 1, pp. 1–8, Dec. 2018, doi: 10.1038/s41467-018-07356-x.
[104] G. Li *et al.*, “Examining Substrate-Induced Plasmon Mode Splitting and Localization in Truncated Silver Nanospheres with Electron Energy Loss Spectroscopy,” *J. Phys. Chem. Lett.*, vol. 6, no. 13, pp. 2569–2576, Jun. 2015, doi: 10.1021/acs.jpclett.5b00961.
[105] M. W. Knight, Y. Wu, J. B. Lassiter, P. Nordlander, and N. J. Halas, “Substrates matter: influence of an adjacent dielectric on an individual plasmonic nanoparticle,” *Nano Lett.*, vol. 9, no. 5, pp. 2188–2192, May 2009, doi: 10.1021/nl900945q.
[106] P. Nordlander, C. Oubre, E. Prodan, K. Li, and M. I. Stockman, “Plasmon hybridization in nanoparticle dimers,” *Nano Lett.*, vol. 4, no. 5, pp. 899–903, May 2004, doi: 10.1021/nl049681c.
[107] “Mie Theory Calculator – nanoComposix.” [Online]. Available: https://nanocomposix.com/pages/mie-theory-calculator#target. [Accessed: 15-Jan-2021].
[108] S. J. Oldenburg, “Light scattering from gold nanoshells,” 2000.
[109] Y. Wang *et al.*, “Substrate-mediated charge transfer plasmons in simple and complex nanoparticle clusters,” *Nanoscale*, vol. 5, no. 20, pp. 9897–9901, Oct. 2013, doi: 10.1039/c3nr02835f.
[110] H. Liu, J. Ng, S. B. Wang, Z. H. Hang, C. T. Chan, and S. N. Zhu, “Strong plasmon coupling between two gold nanospheres on a gold slab,” *New J. Phys.*, vol. 13, Jul.

2011, doi: 10.1088/1367-2630/13/7/073040.
[111] G. C. Li, Y. L. Zhang, J. Jiang, Y. Luo, and D. Y. Lei, “Metal-Substrate-Mediated Plasmon Hybridization in a Nanoparticle Dimer for Photoluminescence Line-Width Shrinking and Intensity Enhancement,” *ACS Nano*, vol. 11, no. 3, pp. 3067–3080, Mar. 2017, doi: 10.1021/acsnano.7b00048.